

1-1-2008

Numerical analysis of the solid particle solar receiver with the influence of an air-jet

Zhuoqi Chen
University of Nevada, Las Vegas

Follow this and additional works at: <https://digitalscholarship.unlv.edu/rtds>

Repository Citation

Chen, Zhuoqi, "Numerical analysis of the solid particle solar receiver with the influence of an air-jet" (2008). *UNLV Retrospective Theses & Dissertations*. 2397.
<http://dx.doi.org/10.25669/1ykp-2btz>

This Thesis is protected by copyright and/or related rights. It has been brought to you by Digital Scholarship@UNLV with permission from the rights-holder(s). You are free to use this Thesis in any way that is permitted by the copyright and related rights legislation that applies to your use. For other uses you need to obtain permission from the rights-holder(s) directly, unless additional rights are indicated by a Creative Commons license in the record and/or on the work itself.

This Thesis has been accepted for inclusion in UNLV Retrospective Theses & Dissertations by an authorized administrator of Digital Scholarship@UNLV. For more information, please contact digitalscholarship@unlv.edu.

NUMERICAL ANALYSIS OF THE SOLID PARTICLE SOLAR RECEIVER WITH
THE INFLUENCE OF AN AIR-JET

By

Zhuoqi Chen

Bachelor of Technology in Electrical Engineering and Automation
Hangzhou Dianzi University, People's Republic of China
2006

A thesis submitted in partial fulfillment
of the requirements for the

Master of Science Degree in Mechanical Engineering
Department of Mechanical Engineering
Howard R. Hughes College of Engineering

Graduate College
University of Nevada, Las Vegas
December 2008

UMI Number: 1463500

INFORMATION TO USERS

The quality of this reproduction is dependent upon the quality of the copy submitted. Broken or indistinct print, colored or poor quality illustrations and photographs, print bleed-through, substandard margins, and improper alignment can adversely affect reproduction.

In the unlikely event that the author did not send a complete manuscript and there are missing pages, these will be noted. Also, if unauthorized copyright material had to be removed, a note will indicate the deletion.

UMI[®]

UMI Microform 1463500

Copyright 2009 by ProQuest LLC.

All rights reserved. This microform edition is protected against unauthorized copying under Title 17, United States Code.

ProQuest LLC
789 E. Eisenhower Parkway
PO Box 1346
Ann Arbor, MI 48106-1346



Thesis Approval
The Graduate College
University of Nevada, Las Vegas

November 21, 2008

The Thesis prepared by

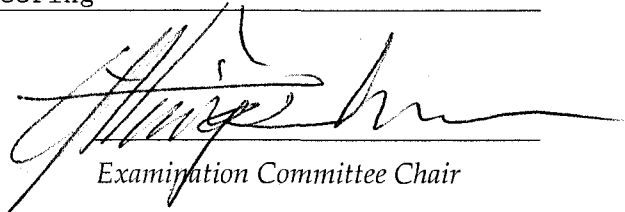
Zhuoqi Chen

Entitled


Numerical Analysis of the Solid Particle Solar Receiver with the
Influence of an Air-jet

is approved in partial fulfillment of the requirements for the degree of

Master of Science in Mechanical Engineering




Examination Committee Chair



Dean of the Graduate College



Examination Committee Member



Examination Committee Member



Graduate College Faculty Representative

ABSTRACT

Numerical Analysis of the Solid Particle Solar Receiver with the Influence of an Air-jet

by

Zhuoqi Chen

Dr. Yitung Chen, Examination Committee Chair
Associate Professor of Department of Mechanical Engineering
University of Nevada, Las Vegas

This thesis develops and analyzes a three-dimensional computational model of a solid particle solar receiver (SPSR) for providing the heat source in a hydrogen production process using the sulfur iodine thermochemical water splitting reaction. In this reaction, a heat input of at least 850 °C is necessary to keep high hydrogen production efficiency. Previous studies to achieve higher efficiency on a SPSR include changing particle materials, sizes, flow rates, and the geometry designs. The present study is concerned with the use of an air-jet in front of the open aperture and different operation conditions for the SPSR design optimization.

The conceptual design of the SPSR is provided by Sandia National Laboratories (SNL). There is an open aperture in front of the receiver cavity, and heat will leak to outside without any protection. Different research topics have suggested that an air-jet consisting of a transparent gas stream injected across the receiver aperture is a good method for isolating the interior from the surroundings. The main purpose of this research

is to use numerical analysis to study the SPSR with the influence of an air-jet. A two-way coupled Euler-Lagrange method is applied which includes the continuity, heat, momentum exchanges between the solid and gas two-phase flows. A two-band discrete ordinate solar ray tracing model is used for the radiation interactions and heat transfer within the particle clouds, and between the cloud and the internal surface of the receiver. Different air-jet velocities are compared to evaluate the thermal performance of the receiver. Parametric studies also include varying particle size, mass flow rate, solar flux, and air-jet temperature to determine the optimal operating conditions. The temperature and velocity profiles inside the cavity are also analyzed. In all the parametric studies and thermal analysis, the SPSR with a downward air-jet velocity of 8 m/s, air-jet temperature of 300 K, and particle diameter in the range of 70-80 micron provides the best performance in the presence of a radiant flux of 920 suns. This cavity efficiency is 85%, and average exit particle temperature is 1199 K.

TABLE OF CONTENTS

ABSTRACT.....	iii
LIST OF FIGURES	vii
LIST OF TABLES.....	ix
NOMENCLATURE	x
ACKNOWLEDGEMENTS.....	xiii
CHAPTER 1 INTRODUCTION.....	1
1.1 Introduction.....	1
1.2 Literature Review.....	5
1.2.1 Experimental Investigations of the Solar Thermal Hydrogen Production and Solar Receiver Design	6
1.2.2 Experimental and Numerical Studies of Gas Flow with Solid Interaction	9
1.2.3 Numerical Method for Turbulence Flow.....	12
1.2.4 Experimental and Numerical Analysis of the 2D and 3D SPSR without Considering the Influence of an Air-jet.....	15
1.2.5 Experimental Research of Material Selection for Solid Particles	20
1.3 Research Objective	22
1.4 Outline of Thesis.....	22
CHAPTER 2 DESCRIPTION OF THE PROBLEM AND GEOMETRY.....	24
2.1 Problem Description	26
2.2 Conceptual Design of Solid Particle Solar Receiver	28
CHAPTER 3 NUMERICAL METHOD AND ALGORITHM.....	29
3.1 Numerical Model Assumptions	29
3.2 Governing Equations and Numerical Model	30
3.2.1 Air Flow Equation.....	30
3.2.2 Turbulence Model	31
3.2.3 Equations of Particles.....	34
3.2.4 Radiation Model.....	35
3.2.5 User Defined Function on the Drag Force	36
3.3 Numerical Modeling Approach	36
3.4 Solution Algorithm	37
3.4.1 Pressure-Velocity Coupling: SIMPLE.....	37
3.4.2 Second-Order Upwind Scheme.....	37

3.4.3 PRESTO Scheme	37
3.4.4 Under-relaxation Factors	38
3.5 Boundary Conditions	38
3.5.1 Pressure Outlet Boundary Condition	38
3.5.2 Velocity Inlet Boundary Condition.....	39
3.5.3 Wall Boundary Condition	39
3.6 Physical Properties Used in the Numerical Model	39
3.7 Mesh Independent Study.....	40
 CHAPTER 4 NUMERICAL SIMULATION OF A THREE-DIMENSIONAL SOLID PARTICLE SOLAR RECEIVER.....	 45
4.1 Comparison of SPSR with and without an Air-jet.....	46
4.2 Parametric Studies of SPSR.....	50
4.2.1 Aerodynamic Analysis of SPSR with Different Air-jet Velocities	50
4.2.2 The Influence of Different Air-jet Temperatures on SPSR	56
4.2.3 Air-jet Injected from the Bottom of Open Aperture	60
4.2.4 The Influence of Different Particle Diameters on SPSR	65
4.2.5 Aerodynamic Analysis of SPSR with Different Particle Mass Flow Rates.....	73
4.2.6 The Influence of Different Solar Irradiation Values on SPSR.....	74
 CHAPTER 5 CONCLUSIONS AND RECOMMENDATION	 76
5.1 Conclusions.....	76
5.2 Future Work.....	78
 REFERENCES.....	 79
 VITA.....	 84

LIST OF FIGURES

Figure 1.1	Simplified schematics of the solar falling particle reactor (FRP) [19].....	11
Figure 1.2	Variation of cavity efficiency and average exit temperature of particles as a function of particle size [29]	17
Figure 1.3	Variation of cavity efficiency and average exit temperature of particles as a function of mass flow rate of particles [29]	18
Figure 1.4	Cavity efficiency as a function of particle size with and without bottom opening [30]	19
Figure 2.1	Schematic of a solid particle solar receiver system [32]	24
Figure 2.2	Conceptual design of a solid particle solar receiver [32]	25
Figure 2.3	Three-dimensional schematic illustration of aerodynamic and thermal behavior in a SPSR with an air-jet	27
Figure 2.4	Two-dimensional schematic illustration of aerodynamic and thermal behavior in a SPSR without an air-jet [32].....	27
Figure 2.5	Conceptual design of the SPSR for the computational fluid dynamics (CFD) study (unit: m)	28
Figure 3.1	The positions of line 1 and line 2, point A and point B	41
Figure 3.2	Velocity magnitude along line 1	42
Figure 3.3	Velocity magnitude along line 2	42
Figure 3.4	Velocity relative error compares to the finest mesh at point A.....	43
Figure 3.5	Velocity relative error compares to the finest mesh at point B	43
Figure 3.6	Computational mesh of the SPSR	44
Figure 3.7	Computational mesh of the SPSR viewed from Y-Z coordinates.....	44
Figure 4.1	Air flow pattern without an air-jet (a) and with an air-jet (b)	47
Figure 4.2	Temperature (K) contours without an air-jet (a) and with an air-jet (b)	48
Figure 4.3	Air flow pattern (a) and temperature contours (b) at slice $x=1$ m. Air-jet velocity is 2 m/s.....	51
Figure 4.4	Air flow pattern (a) and temperature contours (b) at slice $x=1$ m. Air-jet velocity is 4 m/s.....	52
Figure 4.5	Air flow pattern (a) and temperature contours (b) at slice $x=1$ m. Air-jet velocity is 6 m/s.....	53
Figure 4.6	Air flow pattern (a) and temperature contours (b) at slice $x=1$ m. Air-jet velocity is 10 m/s.....	54
Figure 4.7	Cavity efficiencies of SPSR and average exit particle temperatures as a function of different air-jet velocities.....	55
Figure 4.8	Radiation loss and convection loss percentages as a function of different air-jet velocities	56
Figure 4.9	Air flow stream lines released from air-jet. The stream line is colored by temperature. Air-jet velocity is 8 m/s and air-jet temperature is 700 K.....	58

Figure 4.10	Air flow stream lines released from air-jet. The stream line is colored by temperature. Air-jet velocity is 8 m/s and air-jet temperature is 300 K.....	58
Figure 4.11	Air flow stream lines released from air-jet. The stream line is colored by temperature. Air-jet velocity is 8 m/s and air-jet temperature is 500 K.....	59
Figure 4.12	Air flow stream lines released from air-jet. The stream line is colored by temperature. Air-jet velocity is 10 m/s and air-jet temperature is 700 K...	59
Figure 4.13	Air-jet injected from bottom of aperture. The velocity of air-jet is 8 m/s, temperature is 300 K, mass flow rate is 5 kg/s, diameter of particle is 650 micron, and solar flux is 920 suns.....	63
Figure 4.14	Air-jet injected from bottom of aperture. The velocity of air-jet is 8 m/s, and temperature is 700 K, mass flow rate is 5 kg/s, diameter of particle is 650 micron, and solar flux is 920 suns	64
Figure 4.15	Particle volume fraction as a function of distance from back wall at different height in select slice ($x = 1$ m).The diameter of the particles are 200 micron, and air-jet velocity is 8m/s. H is the distance from the bottom wall.....	66
Figure 4.16	Particle volume fraction as a function of distance from back wall at different height in select slice ($x = 1$ m).The diameter of the particles are 650 micron, and air-jet velocity is 8m/s. H is the distance from the bottom wall.....	66
Figure 4.17	Cavity efficiency and average exit particle temperature as a function of particle diameters, velocity of air-jet is 8 m/s, downward air-jet temperature is 300 K, mass flow rate is 5 kg/s, and solar flux is 920 suns.....	68
Figure 4.18	Particle distributions on the bottom plane. Particle size is 200 micron, and air-jet velocity is 8 m/s.	69
Figure 4. 19	Particle distributions on the bottom plane. Particle size is 650 micron, and air-jet velocity is 8 m/s.	69
Figure 4. 20	Particle distributions on the bottom plane. Particle diameter is 100 micron, and air-jet velocity is 8 m/s.....	70
Figure 4. 21	Particle distributions on the bottom plane. Particle diameter is 80 micron, and air-jet velocity is 8 m/s.....	72
Figure 4. 22	Particle distributions on the bottom plane. Particle diameter is 70 micron, and air-jet velocity is 8 m/s.....	72
Figure 4. 23	Particle distributions on the bottom plane. Particle diameter is 60 micron, and air-jet velocity is 8 m/s.....	73
Figure 4. 24	Cavity efficiency and average exit particle temperature as a function of different particle mass flow rates, downward air-jet temperature is 300 K, mass flow rate is 5 kg/s, diameter of particles is 650 micron, and solar flux is 920 suns.....	74
Figure 4. 25	Cavity efficiency and average exit particle temperature as a function of different solar irradiation values, downward air-jet temperature is 300 K, diameter of particle is 650 micron, and mass flow rate is 5 kg/s	75

LIST OF TABLES

Table 1.1	Turbulence models [23].....	13
Table 1.2	Cavity efficiency, average exit temperature of particles, and distribution of heat loss as a function of heliostat field size and cavity size [29]	18
Table 3.1	Operating conditions of gas flow and physical properties of the solid particle	40
Table 4.1	Cavity efficiencies, average exit particle temperatures, heat convection and radiation loss percentages with and without an air-jet	49
Table 4.2	Cavity efficiencies and average exit particle temperatures with different air-jet velocities and different air-jet temperatures	60

NOMENCLATURE

a_λ = spectral absorption coefficient

C_D = drag coefficient

C_p = specific heat capacity (J/kg-K)

c_μ = constant, $c_\mu = 0.09$

c_1 = constant,

c_2 = constant, $c_2 = 1.9$

d_p = the particle diameter (m)

n = the refractive index

G = radiation incident (W/m²)

G_r = Grashof number

g_i = gravity force (m/s²)

$I(\vec{r}, \vec{s}')$ = total intensity

$I_{b\lambda}$ = black body intensity

k = turbulent kinetic energy (m²/s²)

p = pressure (Pa)

Pr = Prandtl number of gas flow

Pr_t = turbulent Prandtl number

$Q_{radloss}$ = radiation heat loss (W)

Q_{inc} = total incident solar energy (W)

$Q_{envloss}$ = convection heat loss (W)

\bar{Q}_p = integrated absorption energy gain of the particles (W)

\bar{Q}_s = the total incident solar energy (W)

\vec{r} = position vector

S = modulus of the mean rate of strain tensor

S_i^M = momentum per unit volume added to the gas phase by the
presence of particles

S_i^T = energy per unit volume added to the gas phase by the
presence of particles.

\vec{s} = direction vector

$u_{i,j}$ = velocity of air flow (m/s)

U_j = mean velocity of air flow (m/s)

u'_j = fluctuant velocity of air flow (m/s)

$u_{p,i}$ = particle velocity (m/s)

Re = Reynolds number

Re_p = relative particle Reynolds number

T = temperature (K)

T_{p-exit} = average exit particle temperature (K)

T_p = particle temperature (K)

\bar{T} = mean temperature (K)

T' = fluctuant temperature (K)

T_R = the radiation temperature (K)

t = time (s)

x, y, z = coordinates

$x_{i,j}$ = coordinates

Greek symbols

α = thermal conductivity (W/m·K)

λ = wavelength (m)

σ = Stefan-Boltzmann constant (W/m²K⁴)

σ_k = constant, $\sigma_k = 1.0$

σ_ϵ = constant, $\sigma_\epsilon = 1.2$

σ_θ = constant, $\sigma_\theta = 0.9$

σ_s = scattering coefficient (1/m)

ϵ = turbulence dissipation (m²/s³)

ϵ_p = particle emissivity (1/m)

η = cavity efficiency

ρ = air density (kg/m³)

ρ_p = particle density (kg/m³)

μ = viscosity (kg/(m·s))

μ_T = turbulent viscosity (kg/(m·s))

ν = kinetic viscosity (m²/s)

ACKNOWLEDGEMENTS

I wish to express my profound gratitude and sincere appreciation to my thesis advisor Dr. Yitung Chen. Throughout my thesis-writing period, he provided encouragement, good advice, patient teaching and lots of inspiring opinions. With his enthusiasm and his great effort to explain things clearly and simply, I can finish my research work and shape my study to this present form.

I would like to send my deep sense of appreciation to my committee members, Dr. Robert Boehm, Dr. Daniel Cook and Dr. Jichun Li. Their critiques and additional suggestions are especially important and helpful for my accomplishment.

To Dr. Taide Tan and Dr. Huajun Chen I would like to thank for their stimulating and endless assistance and guidance from the beginning of my work.

And most importantly, I wish to thank my parents. They raised me up, loved me and taught me never giving up in my life. To them I dedicate this thesis.

CHAPTER 1

INTRODUCTION

1.1 Introduction

Renewable energy like solar, wind, and geothermal resources will become the most important energy supplies for both domestic and world wide consumption in the near future, to eliminate rolling black outs and the increasing cost of energy. People will focus more on the utility part of transforming renewable energy to the form of energies that can be applied to the daily human being activity. The drawbacks to fossil fuel use include limited reserves, and carbon dioxide emissions, which is a greenhouse gas responsible for global warming. Fossil fuel combustion is also responsible for environmental pollution. Hence, the critical part of transforming the energy from a renewable source is to ensure there is no environmental waste or cost for future generations.

Hydrogen, a promising and clean energy carrier, could potentially replace the use of fossil fuels in the transportation sector. The demand for hydrogen is ever growing, with major applications in refinery use and as a component in synthesis gas for manufacture of methanol, ammonia and gas to liquids (GTL) products. Another application for hydrogen in the future will be the fuel cell and internal hydrogen combustion engine for the automotive sector, which could result in a large demand of hydrogen. Currently, no environmentally attractive, large-scale, low-cost and high-

efficiency hydrogen production process is available for commercialization [1]. Hydrogen is an important reactant and an energy carrier that can be manufactured from a range of energy sources such as fossil fuels, biofuels, renewable energy, and nuclear energy via electricity [2]. Today's hydrogen production is mainly based on fossil fuels and most specifically on natural gas [3]. There are no environmental benefits if the hydrogen is derived from natural gas or fossil fuel reforming, because of the emissions of CO₂ from these production routes.

The use of wind, hydropower and solar thermal energy for the production of hydrogen are the most environmental friendly methods. The solar-driven water-splitting thermochemical cycles may constitute the optimized choice for hydrogen production. Many cycles can be selected for the production of hydrogen from splitting water, and most of them need a reaction temperature in the range of 850-2000 °C. The sulfur-iodine and hybrid sulfur processes are two examples of the hydrogen production process having a maximum temperature of around 850 °C [4], [5] which can be supplied by nuclear or solar energy. Reactions that need more energy input, like the zinc-oxide [6] process, require heat input at temperature of 2000 °C. The only energy supply which can reach this high temperature is from solar energy.

As energy prices have increased, engineers have focused more on the overall cost of fuel. One benefit for using renewable energies is their unlimited resource, so operating cost becomes the most important part of the total energy production process. There are several designs for producing hydrogen by using renewable energy as the heat source, and one of them is through using solar energy. Hydrogen could be produced by thermochemical water-splitting, a chemical process that consists of the multistep

decomposition of water. Water and heat are the inputs, and hydrogen and oxygen are the only outputs. The other chemicals and reagents are recycled in a closed cycle. The heat can be applied using nuclear energy, but it is much more environmentally acceptable if the heat source is solar energy. One problem with using solar energy is although the solar radiation is a high quality energy source, its power density at the earth's surface makes it difficult to extract work and achieve reasonable temperatures in a working medium. Therefore, solar thermal energy must be collected by concentrated methods.

Concentrated solar energy can be collected by a solar central receiver system which uses mirrors (large scale of heliostat field) to reflect and focus sunlight onto a receiver located on top of a solar tower. In this manner the collected sunlight can reach hundreds of suns at the surface of the solar receiver. The concentrated solar energy is capable of attaining the temperature requirement for the thermochemical reaction cycle at 2000 °C.

A working medium is needed to transport the energy for the reactions that need a heat source. Previous studies on the working medium in a solar central receiver have been on gases or liquids which need to be transported by tubes or pipes. There are working demonstrations of systems using liquid as the heat medium like the water/steam central receiver system, located near Barstow, California, which produces electrical energy [7]. The other common working fluids are molten salts, molten metals, and air.

The term solid particle solar receiver is another concept of a heat energy transfer medium with great interest. Sand-size refractory particles fall down freely inside a solar receiver to form a curtain that directly absorbs the solar insolation. The advantages of using a solid particle receiver over the systems of gas/fluid mediums are: (1) the solid

particles can absorb the reflected and concentrated solar energy directly, eliminating the pipes or tubes used to transport the fluids, (2) solid material might reach higher temperature, (3) solid particles can be a heat storage medium, eliminating the need for extra elements in the storage system [8].

The solid particle solar receiver turns out to be an attractive choice as the heat source for hydrogen production. Most solid particle receivers have an open aperture in front of the cavity where the concentrated solar light can pass through, but a large amount of heat might be lost from there by convection and radiation. The reasons for abandoning the transparent window to cover the open aperture are that materials that endure high temperature are not readily available, and the solid particles are very light and small and will stick on the window when spreading inside the cavity, reducing the window transparency. In this thesis, an air-jet consisting of a transparent gas stream injected across the aperture to isolate the interior from the outside was used. The benefit is the elimination of convection heat loss [9].

An air-jet is used routinely as a thermal barrier for warehouse doorways and department store entrances. For the aperture of the SPSR, the commercial air-jet is applicable for the whole system in the application methods, and the cavity efficiency will increase by the insulation of the interior from the ambient environment. On the other hand, the fluid dynamic behavior is very complicated inside the whole system, especially when coupled with the air-jet and characteristics of the particles.

In the engineering world, computational fluid dynamics (CFD) is a useful numerical tool for the analysis of problems which involve fluid flow and heat transfer. High requirements for computer performance are needed during the calculation process.

The most fundamental consideration in CFD is treating the continuous fluid in a discretized way, by dividing the domain into small meshes or grids. Then, it is necessary to apply meshes into a suitable algorithm to solve the equations of continuity, motion, energy, and species. Compared to experimental research, CFD analysis provides a simulation environment for each case without wasting material and time, which is expensive and unpredictable. Continuous flow is complicated by unstable flow patterns, so different kinds of conditions and models can be applied to solve these problems using CFD analysis. The aerodynamic behavior inside the solid particle solar receiver can be evaluated by this computational tool.

1.2 Literature Review

The solid particle solar receiver studies started about 20 years ago. There are plenty of researchers considering methods of hydrogen production by splitting water or other chemical reaction routines. These kinds of processes require very high temperature input as the heat source to realize the optimized design for the whole hydrogen production system. Solar energy is an unpolluted and high temperature heat supply. For engineers, the design of collecting the energy is very important. In some designs, the heat absorbing and reaction progress occur in the same place [3-6]. In this present design, the SPSR is only used as a heat absorbing device. Solid gas two-phase flows can happen in several design domains, and will be discussed in this review. Also, the properties of materials for solar absorptions were experimentally studied by SNL. In the simulation section, different modeling results for the radiation, heat convection and turbulence flow from other researchers are reviewed.

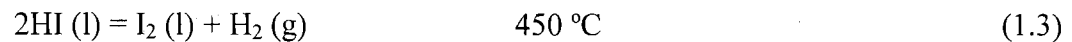
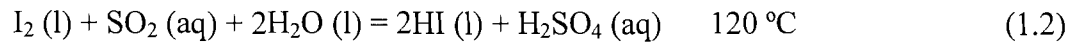
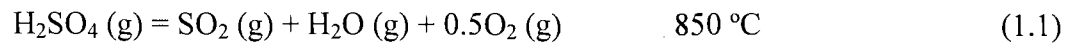
1.2.1 Experimental Investigations of the Solar Thermal Hydrogen Production and Solar Receiver Design

Different designs of concentrated solid particle receivers were used as solar energy collectors or both solar energy collectors and thermochemical reactors. Inside this receiver cavity, solid gas two-phase flows are analyzed. The design of a concentrated solid particle receiver depends on the temperature requirement of the reaction cycle and the desired system working efficiency.

Life cycle assessment (LCA) of hydrogen production was first considered by Koroneos et al. in [3]. In his research, LCA is a powerful tool to help evaluate the impact from a process or from production and use of a product. It consists of goal definition and scoping which defines the product, process or activity; inventory analysis which identifies material usage and environmental releases; impact analysis which assesses the human and ecological effects of energy, water and material usage; and last interpretation, which evaluates the results of each analysis. The research compared hydrogen production by natural gas, renewable energy, electrolysis, and fuel. The use of wind, hydropower, and solar thermal energy were proven to be the most environmentally friendly and efficient methods. And the future of renewable hydrogen energy depends strongly on reduced costs for renewable energy production.

The methods of collecting renewable energy such as solar thermal energy for hydrogen production are concluded by some scientists. Stephane summarized a database of water-splitting thermochemical cycles [1]. All selections and evaluations of promising thermochemical reaction cycles were performed in the temperature range of 850-2000 °C. Process temperature, process complexity, and energy analysis of thermochemical cycles

were used as the standards for efficiency, and the sulfur-iodine (S-I) cycle was the cycle with the highest reported efficiency (52%). It was suggested, that with process improvements, it was possible to increase the efficiency and lower the capital cost [10] [11]. The S-I cycle consists of three reaction steps [12]:



The cycle can be separated into four sections:

- I. Acid production and separation with oxygen purification,
- II. Sulfuric acid concentration and decomposition,
- III. Hydroiodic acid (HI) concentration,
- IV. HI decomposition and H_2 purification

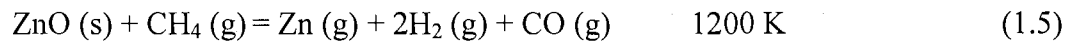
Section II of the cycle is an endothermic reaction driven by the heat input from a high temperature source. The utilization of nuclear power and solar energy can be considered as the temperature heat source in this step [13]. William A. Summers has researched nuclear hydrogen production based on the hybrid sulfur thermochemical process [5]. This requires two sulfur cycles – the sulfur-iodine and the hybrid sulfur. The second thermal decomposition requires a heat input of 800-900 $^\circ\text{C}$, which is provided by nuclear reactors. Process design studies suggest that a net thermal efficiency of over 50% is possible with this hydrogen production cycle. The heat input required to drive the solar thermal reaction was provided by the solar reactor as a cavity receiver. Several designs for these kinds of thermal reactions involving gas and solids are introduced in the following paragraphs.

The solid particle solar receiver has been designed as the main component for the gas-solid thermochemical reactions in Steinfeld's research [14]. In his work, the reaction of interest is characterized by the equation:



This reaction will go spontaneously to the right at temperature above 1170 K and 1 atm. As the reaction system is complicated by the heterogeneous reactants and products which need to be removed, separated, and fed, the feature of both the solar receiver and reactor need to be combined. Incoming concentrated solar radiation enters the cavity without any window protection, because windows for solar receivers are usually expensive, brittle, require careful mounting, but often fail to withstand the high solar fluxes and high temperature, reducing the solar energy absorption efficiency. The experimental set-up is done, and the peak flux concentration ratio observed was 1410 suns (1 sun = 1 kW/m²). The reactor in the solar furnace with the CaCO₃ decomposition reaction reached 1300 K and obtained high degree of calcination. The energy absorption efficiency, based on the energy incident on the receiver aperture, was 43 % [14].

The production of zinc by reduction of zinc oxide and refining of CH₄ is characterized by the high energy consumption, using solar thermal energy as energy source to cause the following reaction:



This reaction is studied in a solar receiver consisting of a fluid-bed reactor and a compound of parabolic concentrators. The ZnO particles are directly irradiated, fluidized in CH₄, and acted as heat absorbers and reactants. The produced Zn vapor was trapped in

a condenser, and synthesis gas containing a 2:1 mixture of H₂ and CO is collected, without discharging greenhouse gases and other pollutants. This is a relatively environmentally clean path for either recycling Zn-air or producing H₂ in a water-splitting scheme [15]. The production of Zn from ZnO in high temperature can be used to split water to hydrogen in an exothermic reaction [16], and the by-product of ZnO can be recycled to the solar process.

Another study analyzed the radiation heat transfer in a solar chemical reactor for the co-production of hydrogen and carbon by thermal decomposition of CH₄.



The solar chemical reactor features a vortex flow of CH₄ with the participating of solid carbon particles to serve both as the heat absorber and the reaction catalyst. Hirsch [17] developed a three-dimensional reactor model to predict the energy, temperature and chemical reaction inside the solid particle cavity. Different parameter inputs like particle size and solar loading were validated to improve the overall reaction efficiency.

1.2.2 Experimental and Numerical Studies of Gas Flow with Solid Interaction

Computational fluid dynamics (CFD) was employed in the design and optimization of a high temperature central receiver or reactor, which combined the gas-solid flows inside. Experimental works accompany the simulation results to identify the characteristics of the two-phase flows.

The fluid flow, particle transport, and heat transfer of a high-temperature solar chemical reactor was studied by Meier et al. [18]. The reactor consists of a cylindrical cavity and an open aperture through which concentrated solar radiation enters. The particles (reactants) impinge on a cone and are conveyed in a swirling air stream. A

general purpose CFD code was used to simulate the fluid flow and heat transfer in the particle-cloud reactor. The governing Navier-Stokes equations were solved by a ‘hybrid’ differencing scheme. The semi-implicit method for pressure-linked equations consistent (SIMPLEC) velocity-pressure coupling algorithm is used. Since the conventional $\kappa - \varepsilon$ turbulence model always fails to predict swirling flow correctly, a renormalization group modification of the standard high Reynolds number version of the $\kappa - \varepsilon$ turbulence model was applied. The motion of particles in the air flow was modeled using a discrete trajectory (Lagrangian) approach. An iterative process was needed to adjust the coupling between the particle transport and the fluid flow. Heat transfer and particle flow pattern were presented in this research to evaluate the performance and validate the experimental results.

In another work, Meier [19] used the thermal heat from a falling particle receiver/reactor which exposed to concentrated sunlight to decompose limestone (CaCO_3). In this case, concentrated solar radiation is absorbed directly by a curtain of free-falling solid particles that were heated to temperatures in excess of 1200 K over approximate 5 m fall in the presence of a radiant flux of less than 1 MW/m^2 . The simple schematic of the solar falling reactor is shown in Figure 1.1. For this study, the general purpose CFD code CFX-4 was used, the gas/particle flow and the convective heat transfer in the solar falling particle reactor (FPR) were modeled within the CFX-4 solver, and particle heating by radiation was calculated in the CFX-RADIATION model using a Monte Carlo method. Input parameters and results from CFD simulations of the FPR are compared. The model was verified with experimental data and an improved design of the FPR was mentioned there.

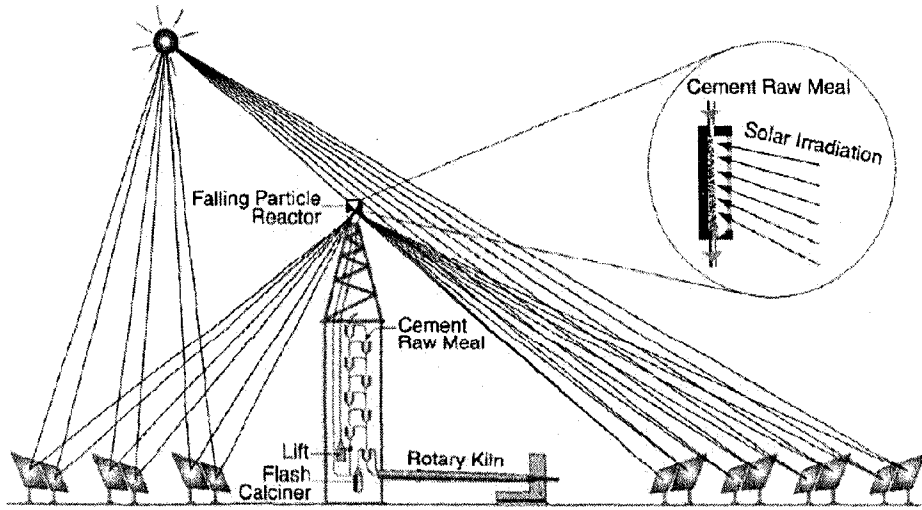


Figure 1.1 Simplified schematics of the solar falling particle reactor (FRP) [19]

A detailed recent study about the two-phase flow gave insight about the radiation characteristics of particles, which are approximated using seeded particles of variable size and shape [20]. It proved that radius of limestone less than 100 micron is inefficient in absorbing solar energy. In present study of SPSR, the solid particle used has a higher heat capacity ($C_p = 1085 \text{ J/kg-K}$) than limestone ($C_p = 840 \text{ J/kg-K}$). So particles with radius less than 100 micron still can perform with high efficiency in this study of SPSR. Different from previous studies, molecular particle collisions were considered in the energy transfer. The receiver simulations were performed by the commercial CFD code PHOENICS, coupled with two radiation transfer solvers. A swirl model was added to the standard PHOENICS code to simulate the tangential flow in the receiver. And a Monte Carlo ray-tracing method was used to introduce the irradiation incident on the aperture plane. The receiver simulations showed good agreement with the wall temperature distribution that measured in experiment. Due to the limitation of the simulation code and model, gas exit temperature was significantly lower than the measured value.

There are other models for the simulation of two-phase flow created in the 1970-80's, which were based on one-dimensional or two-dimensional geometries and were relatively simple. In Crowe et al.'s [21] research of gas-droplet flows, a particle-source-in-cell (PSI-CELL) model was used to illustrate the capability of the model to treat the complex phenomena associated with multiphase flows. Raithby introduced a "finite-volume" method to predict radiant heat transfer in enclosure with participating media [22]. This method conceptually used the same nonorthogonal grids to compute fluid flow and heat transfer. The results have been benchmarked and have shown good accuracy.

1.2.3 Numerical Method for Turbulence Flow

In engineering practice, flow in three dimensions like pipes, cavities and wakes, will become complicated when the Reynolds number is higher than a certain value. This is observed as turbulent flow, a chaotic and random state of motion that develops in which the velocity and pressure change continuously with time and within substantial regions of flow [23].

A turbulence model can be used by calculating the mean flow, so that less variety of flow problems can be calculated. A turbulence model must be applicable to the general CFD code and be accurate, simple, and economical to run. The most common turbulence models are classified in Table 1.1. This table is divided into classical models and large eddy models. In this review, much more attention is paid to the numerical and experimental variability of the two-equation $\kappa - \varepsilon$ model.

Table 1.1 Turbulence models [23]

Classical Models	Based on Time-Averaged Reynolds Equations
	<ol style="list-style-type: none"> 1. zero equation model - mixing length model 2. two-equation model - $\kappa - \varepsilon$ model 3. Reynolds stress equation model 4. algebraic stress model
Large Eddy Simulation	Based on Space – filtered Equations

Jones used a two-equation model for the prediction of turbulence flow early in the 1970's [24]. In the two-equation turbulence model, the turbulent viscosity is determined from the solution of transport equations for the turbulence kinetic energy and the energy dissipation rate. In high Reynolds number flow, the turbulence energy and energy dissipation can be written as:

Turbulence energy:

$$\rho \frac{D\kappa}{Dt} = \frac{\partial}{\partial y} \left(\frac{\mu_T \partial \kappa}{\sigma_k \partial y} \right) + \mu_T \left(\frac{\partial u}{\partial y} \right)^2 - \rho \varepsilon \quad (1.8)$$

Energy dissipation:

$$\rho \frac{D\varepsilon}{Dt} = \frac{\partial}{\partial y} \left(\frac{\mu_T \partial \varepsilon}{\sigma_\varepsilon \partial y} \right) + c_1 \frac{\varepsilon}{\kappa} \mu_T \left(\frac{\partial \mu}{\partial y} \right)^2 - c_2 \frac{\rho \varepsilon^2}{\kappa} \quad (1.9)$$

The turbulence viscosity is defined by $\mu_T = c_\mu \rho \kappa^2 / \varepsilon$. The terms c_μ , c_1 , c_2 , σ_κ , and σ_ε are empirical constants, the values of which are defined in the high Reynolds number form of the $\kappa - \varepsilon$ model of turbulence.

Later on, a model for numerical simulation of buoyant, turbulent flow was developed by Humphrey et al. [25] [26]. The first part corresponds to free convection along a heated vertical flat plate, and the second part extends to predict steady free and mixed convection flows of air in a strongly heated cavity of arbitrary rectangular cross-section and orientation. Both cases consider the numerical simulation of more complex, buoyancy-affected, turbulent flows. Two low Reynolds number turbulence model formulations had been developed for predicting wall-bounded, variable property, free convection flows. The KEM model (commonly referred to as the $\kappa - \varepsilon$ model) relates turbulent fluxes to eddy viscosities via a generalized Boussinesq hypothesis. The latter approach involves partial differential equations for the turbulence corrections. Truncation of these transport equations, obtained by neglecting convection and diffusion terms, yields a system of algebraic equations relating the turbulent fluxes to known or calculable flow quantities; the terminology algebraic stress model (ASM) is applied to describe the method. In the second part of these studies, the characteristics of the flow depend on the cavity aspect ratio, a/b , the inclination angle, α , and the Grashof number, Gr . Prediction of the Nusselt number Nu for the mixed convection flow is important when considering the influence of buoyant force, and it is characterized by Re^2/Gr . For both free and mixed convections, the predicted flow patterns are in good qualitative agreement with the flow profiles in experiments.

Ince et al. [27] give another example of the calculation of buoyancy-driven turbulent flows in rectangular enclosures under the two cases of different aspect ratios, 30:1 and 5:1. A version of the Jones-Launder low-Reynolds-number $\kappa - \varepsilon$ model with the modified coefficient was used. The turbulent stresses and heat fluxes are given by:

$$\overline{\rho u_i u_j} = \frac{2}{3} \delta_{ij} \rho \kappa - \mu_T \left(\frac{\partial u_i}{\partial x_j} + \frac{\partial u_j}{\partial x_i} \right) \quad (1.10)$$

$$\overline{\rho u_j T} = - \frac{\mu_T}{\sigma_\theta} \frac{\partial T}{\partial x_j} \quad (1.11)$$

Here $\mu_T = C_\mu \rho \kappa^2 / \varepsilon$, the turbulence energy κ and ε part of energy dissipation rate terms that are obtained from their own transport equations. The numerical results lead to a satisfactory agreement with reported experimental data.

A new $\kappa - \varepsilon$ model consists of a new dissipation rate equation and a new realizable eddy viscosity formulation is used for high Reynolds numbers turbulent flows [28]. Results of this model are compared with available experimental data and the results from a standard $\kappa - \varepsilon$ model, and it presents a significant improvement in the following types of flows:

- i. Rotating homogeneous shear flows;
- ii. Boundary-free shear flows including a mixed layer, planar and round jets;
- iii. A channel flow, and flat plate boundary layers with and without pressure gradient;
- iv. Backward facing step separated flows.

1.2.4 Experimental and Numerical Analysis of the 2D and 3D SPSR without Considering the Influence of an Air-jet

The research and development of a SPSR was conducted within the U.S Department of Energy (DOE) as a part of the Solar Hydrogen Generation Research program. Experiments on the design, and material testing, have been conducted by SNL since the 1980's. In initial research, Evans et al. [29] mentioned numerical modeling of a

SPSR. They studied the flow of air and particles with combined heat transfer inside a solar heated, open cavity containing a falling particle curtain. Two-way momentum and thermal coupling between the particles and the air was included in the analysis, along with the effects of radiative transport within the particles, between the heated gas and particle surface. This was a two-dimensional steady flow design, and the PSI-Cell (particle source in cell) computer code was used to describe the gas-particle interaction. The radiative heat transfer characteristics within the particle clouds were obtained using a discrete ordinate method. From the experimental work, particles were diluted as they were falling down, and the volume fraction of particles was small enough to ignore the particle-particle collisions. Pressure-velocity coupling was determined by using the revised procedure of semi-implicit method for pressure-linked equations (SIMPLER), and differential equations of describing turbulent energy κ and dissipation ε were solved. In the analysis of the aerodynamic behavior of the SPSR, the authors considered the interaction of particle-particle radiation, particle-wall radiation, particle-air convection and air-wall convection. The properties like scattering, thermal emission, and wavelength dependence of the particles are accounted for in the radiation model calculation. Geometry of the two-dimensional design was a 6.7 m by 5.0 m cavity. Nominal parameters in this research were incident solar energy of 920 suns, particle diameter of 650 microns, particle mass flow rate of 5.4 kg/s, and initial particle temperature and downward velocity of 293 K and 0.3 m/s. In the parametric studies of the receiver behavior, the mass flow rate, particle diameter, particle infrared scattering albedo, and absorptivity are varied independently to determine their efficiency and particle exit temperature.

The results identified that smaller particles can provide better performance, as shown in Figure 1.2, due to a greater *optical thickness* and *longer residence time*. Increasing the particle mass flow results in an increase in cavity efficiency with a decrease in particle temperature, as shown in Figure 1.3. Solar flux intensity is a value that depends on the heliostat area and receiver aperture dimension of the cavity. In this two-dimensional design, cavity efficiency, average exit temperature of the particles, and distribution of the thermal losses under the influence of different solar flux data are compared in Table 1.2.

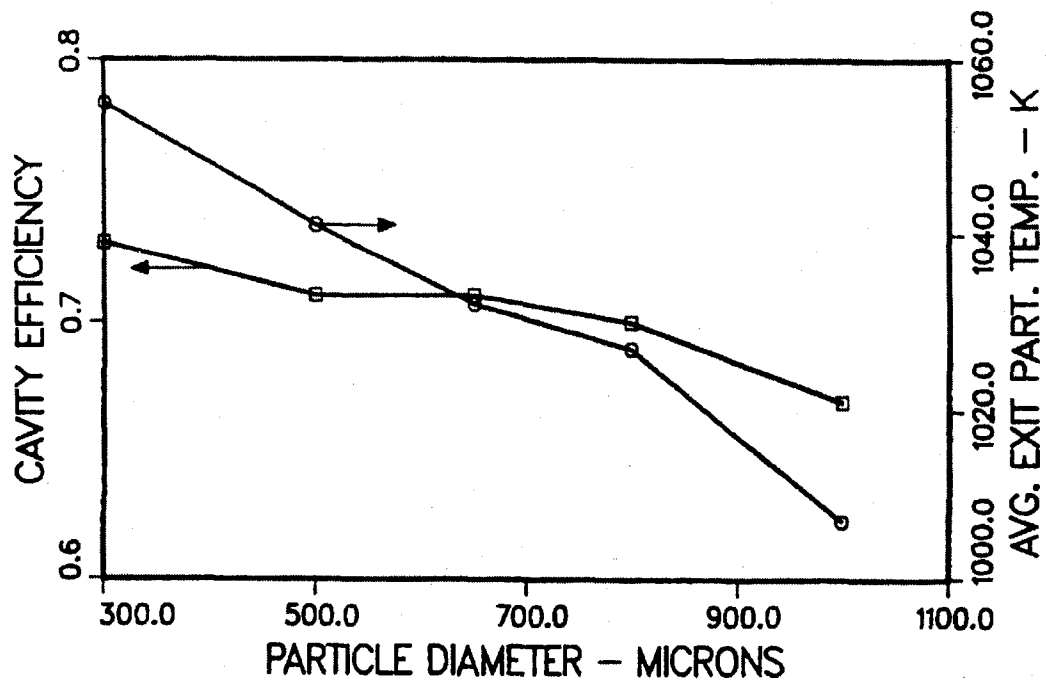


Figure 1.2 Variation of cavity efficiency and average exit temperature of particles as a function of particle size [29]

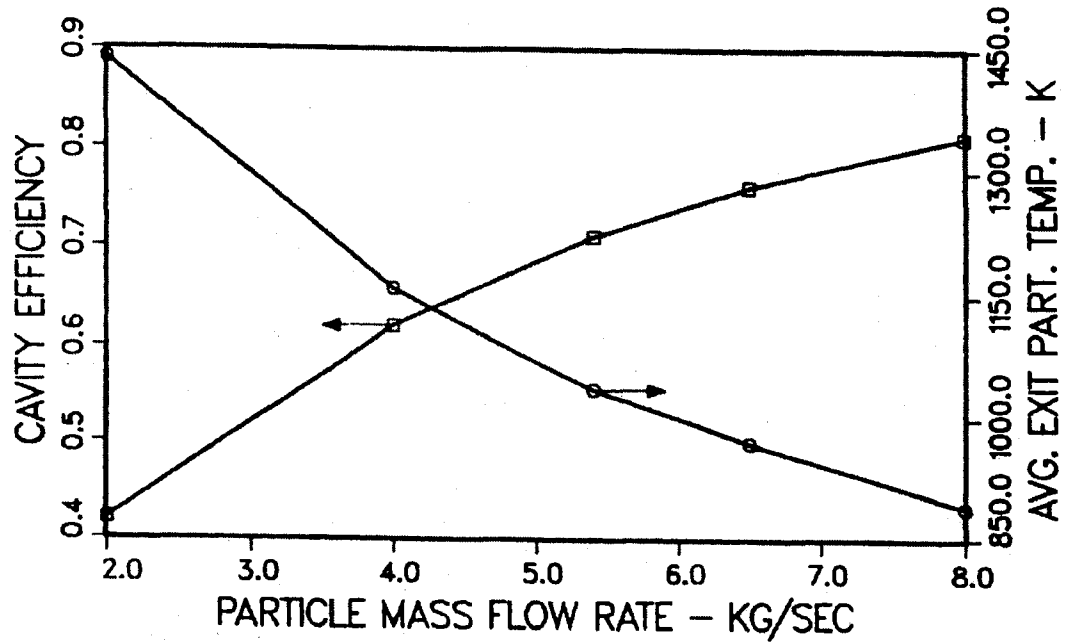


Figure 1.3 Variation of cavity efficiency and average exit temperature of particles as a function of mass flow rate of particles [29]

Table 1.2 Cavity efficiency, average exit temperature of particles, and distribution of heat loss as a function of heliostat field size and cavity size [29]

Field Size (m ²)	Average Flux (suns)	η	T _{p-exit} (K)	$\frac{Q_{radloss}}{Q_{inc}}$	$\frac{Q_{envloss}}{Q_{inc}}$
10 ⁴	790	0.59	930	0.29	0.11
10 ⁴	1280	0.70	1032	0.22	0.08
10 ⁵	650	0.59	932	0.11	0.28
10 ⁵	650	0.64	973	0.09	0.26
10 ⁵	920	0.70	1032	0.10	0.19
10 ⁵	1530	0.86	1175	0.07	0.07

Later, the aerodynamic and thermal interaction between gas flow and solid particles in a detailed three-dimensional design was investigated by Chen et al. [30]. Improved simulation tools for the modeling were applied in this research. The working media for the solid particles was bauxite and includes ~7% iron oxide. Realizable $\kappa - \varepsilon$ turbulence model and solar ray tracing algorithm were used to evaluate the model. Figure 1.4 shows parametric studies on the performance of the SPSR with and without bottom opening, and less convective loss between particle and entrained air flow can be achieved without a bottom opening. Compared with larger diameter particles, particles with smaller size are easier to heat and can achieve a higher temperature.

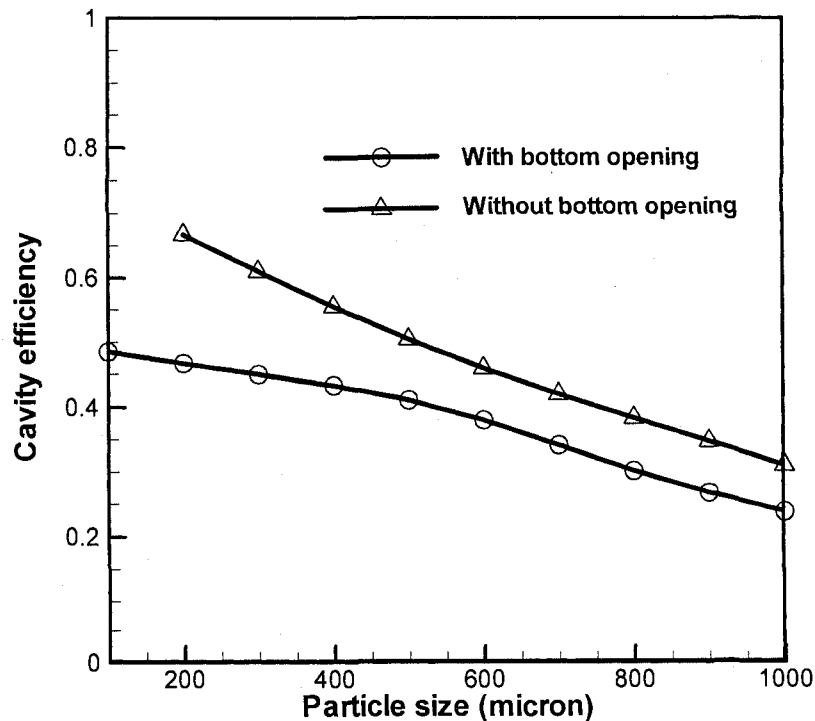


Figure 1.4 Cavity efficiency as a function of particle size with and without bottom opening [30]

Increasing of the particle mass flow rate can also improve the cavity efficiency evidently. The performance of the SPSR can be enhanced by assuming that there is no bottom opening, and in practical applications, it can be realized by applying a hopper to collect these falling particles.

1.2.5 Experimental Research of Material Selection for Solid Particles

Particle material selection is the most important topic in the technical studies. The design of the SPSR is based on the understanding the behavior of the free falling particles, such as the agglomeration, fracture and optical properties of the particles. Several characteristics of different materials are compared by Abdelrahman et al. [31], and Hruby [32] [33]. They also mentioned the different methods that were used to analyze the behaviors of these particles.

The characteristics of the particles were first investigated in the study of solid-gas-suspensions, which is used for direct absorption of concentrated solar radiation [31]. This study makes the choice of appropriate type of particles for any further studies on the solar direct absorption particles. It considers the appropriate diameter in gases, and also absorptivity and emissivity in the IR range were investigated. Early in 1908, a classic equation for the optical behavior of spheres of any size or material that subjected to radiation was derived [34]. And this theory was used for finding out the important factors influencing the particle numerical calculation. For a given concentration and optical depth, the absorptivity depends on its complex index of refraction in a specific wavelength. This study showed that graphite is a suitable material from these optical properties and availability.

In Hruby's [32] technical feasibility studies of the solid particle behavior, the author points out that particle velocity and volume fraction are the two most important parameters for characterizing the aerodynamic behavior of a free-falling particle cloud. And in the material selection, agglomeration, fracture resistance and optical properties of alumina, silica, silicon carbide and zircon were compared. Agglomeration investigations indicated that alumina, silica, and zircon have the best performance of pure ceramic material for use between 1000 and 1200 °C. Impact-induced fracture was not a problem for the small, round particles. Bulk solar absorptivity investigation identified that the candidate material which performs best in agglomerating had low solar absorptivities. As a result, more materials needed to be tested. Two particle materials were chosen to examine under this situation. They are:

1. Master Beadtm is an alumina based particle,
2. Zirproptm is a zircon-silica (zirconia) based particle.

The results indicate that Master Beadtm is a candidate as a solid particle material at temperature up to 1100 °C. At temperatures above 1000 °C, an applied pressure will cause it to agglomerate. Zirproptm does not agglomerate at temperatures up to 1200 °C under applied pressure. However its absorptivity decreases as the temperature increases.

The working media for a SPSR is commercially available for purchase from CarboHSP according to recent research [13]. A schematic design of the drop test platform shows the material's properties with sphericity of 0.9, roundness of 0.9, and diameter of 697 micron. The solid volume fraction is measured by a circuit. Blacklit images are taken to evaluate the opacity of the curtain. From this study of particles, the particle-particle

collision can be neglected in future calculations, because the solid volume fraction is very small [35].

1.3 Research Objective

A conceptual design of a SPSR and on-sun test has been proposed by SNL. The objective of this research is to create a detailed three-dimensional model for a SPSR with the influence of an air-jet. The aerodynamic behavior of the particles and thermal interactions which include particle-particle radiation, particle-wall radiation, particle-air convection, and air-wall convection are investigated in this research. The parametric studies are aimed to evaluate the optimal performance of the SPSR. Numerical results obtained from the numerical model include the fluid flow pattern, heat transfer behavior inside the cavity, average exit particle temperature and cavity efficiency. Conclusions are drawn from these results and intended for use in further studies to improve the design of the SPSR.

1.4 Outline of Thesis

A three-dimensional conceptual design of the SPSR and details of the simulation models are discussed in this work. Chapter 2 gives a description about the problem and the numerical modeling tools which are applied in the conceptual design. The whole system is described on a conceptual basis, which is also introduced in Chapter 2. In this research, all the numerical methods and algorithms are introduced in Chapter 3. Several assumptions are made to analog the working environmental of the SPSR. In Chapter 4, the results of model of the SPSR with the influence of an air-jet are discussed, and

different parametric studies are presented to find an optimized design for the model. At last, in Chapter 5, conclusions and recommendations from this research are pointed out to provide suggestions on the design work of hydrogen production from a SPSR energy source system.

CHAPTER 2

DESCRIPTION OF THE PROBLEM AND GEOMETRY

SNL provided the conceptual design of a SPSR and schematic of this energy source supply and collecting system. The experimental research of the whole system was also developed by SNL. Figure 2.1 [32] shows the solid particle receiver system design, which contains the particle lift system, hot particle storage system, direct contact heat exchanger, and lower temperature solid particle storage system. The main focus of this thesis is on the design of the solid particle receiver part as shown in Figure 2.2 [32].

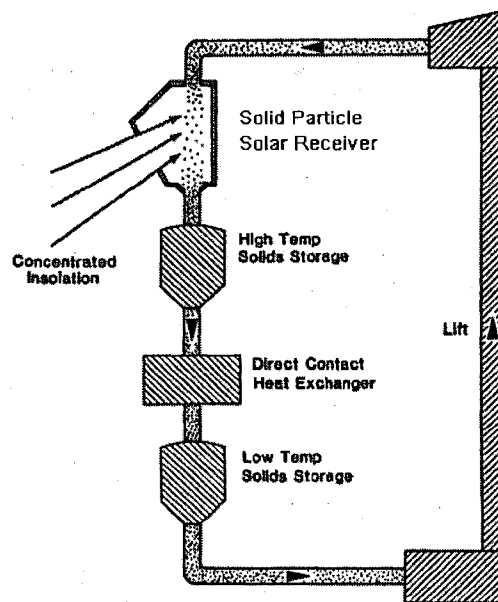


Figure 2.1 Schematic of a solid particle solar receiver system [32]

Other components of the system are considered less important than the SPSR, but are with particular interests to improve the efficiency of the whole system. The particle lift system needs to move the solid particles from ground level to the top of the receiver, and promise the particle initial temperature won't below requirements before falling down from the top. Agglomeration and fracture should be prevented when the high temperature particles rest in the hot tank. These depend on both the particle material selection and design of the storage component. After particles are transported through the heat exchanger, a temperature of minimum requirement for hydrogen production reaction must be confirmed. In the hydrogen production system, a large amount of heat transfers through each component. A reasonable design can reduce the loss of heat energy and get a better performance from the SPSR.

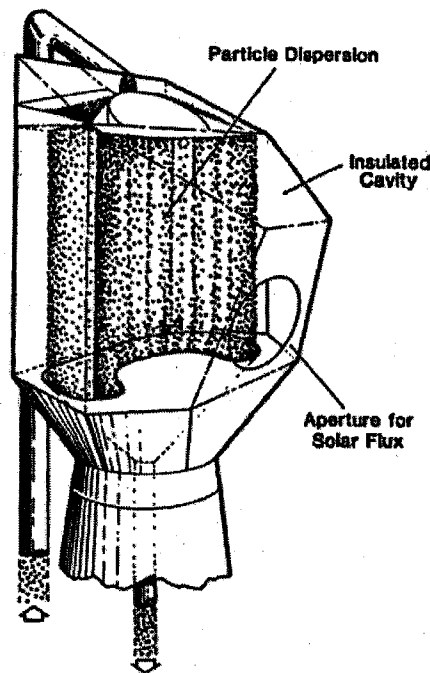


Figure 2.2 Conceptual design of a solid particle solar receiver [32]

Aerodynamic and thermal behaviors of the free-falling particle cloud were studied, aimed at evaluating the performance of the SPSR. Experimental work of particle falling behavior concluded that particle volume fraction was small, less than 1% [29]. Under this condition, particle-particle collisions can be neglected, because particles were diluted in free fall.

2.1 Problem Description

Figure 2.3 shows three-dimensional schematic illustration of a SPSR with heated particles under the influence of an air-jet. The particles are pouring down from the top of the cavity to form a curtain which can absorb the solar irradiation directly. Air entrainment was shown to be important in experimental work of Evans et al. [29] and Koroneos et al. [3], in which the velocity of the particles was significantly higher on the terminal values, corresponding to an isolated particle falling in a quiescent environment. A buoyant force is generated because air beside the particle curtain is warmed up by the heated particles. This results in an increase in the particle residence time, which helps each particle to remain within the radiant flux field for a longer period.

In the case without an air-jet, as shown in Figure 2.4, warm air leaks from the top, and cold air sucks from downside through front aperture. If an air-jet is blowing vertically downward and cross the aperture, as shown in Figure 2.3, the inside gas-solid flow pattern and heat energy of cavity can be considered as being well protected. There exists an optimizing velocity working value of the air-jet, smaller than which heat generated by the particles can also leak from the bottom of the aperture, and larger than that value will become a waste of energy input.

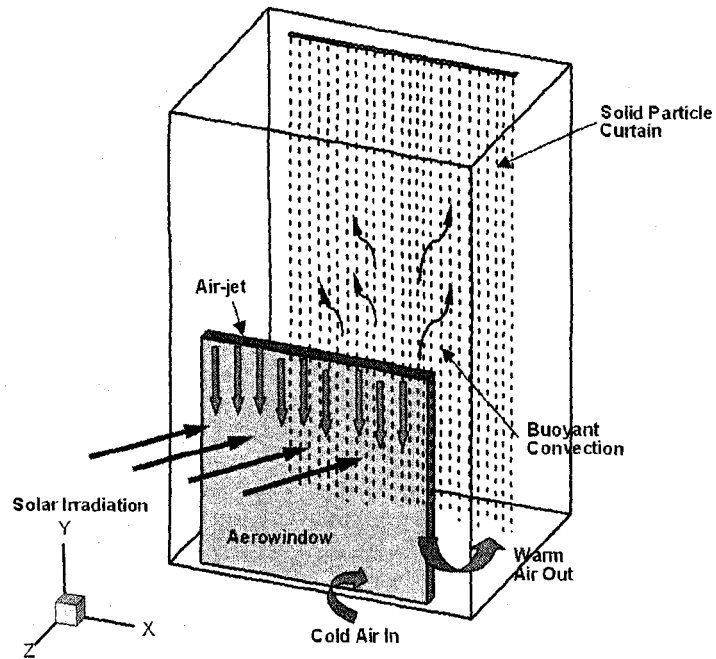


Figure 2.3 Three-dimensional schematic illustration of aerodynamic and thermal behavior in a SPSR with an air-jet

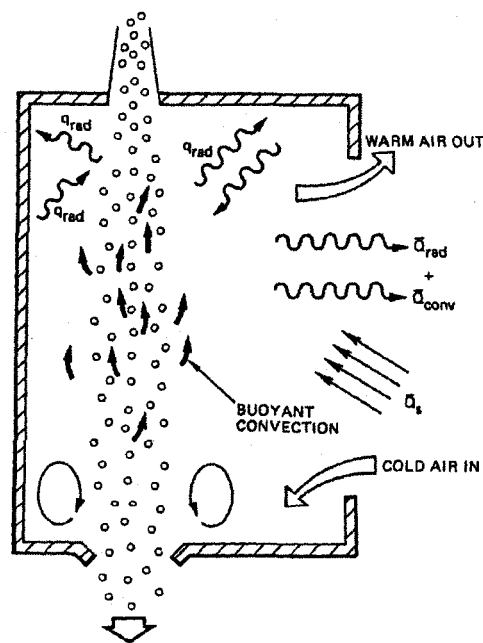


Figure 2.4 Two-dimensional schematic illustration of aerodynamic and thermal behavior in a SPSR without an air-jet [32]

2.2 Conceptual Design of Solid Particle Solar Receiver

The SPSR geometry and dimensions are shown in Figure 2.5. This is the conceptual design for the SPSR that may be constructed by SNL for experimental verification. Our research objective is to prove numerically that the design can achieve a high exit particle temperature ($>850\text{ }^{\circ}\text{C}$), which is needed for the heat supply of the sulfur-iodine thermochemical process. The geometry of the SPSR consists of a rectangular cavity that is 2 m in width, 1.58 m in depth and 3 m in height. On the top of the cavity, an opening of 0.25 m by 1.5 m is used for introduction of the particles. An area of 1.5 m by 1.5 m square is the open aperture in front of cavity, from the top of which an air-jet will blow downwards.

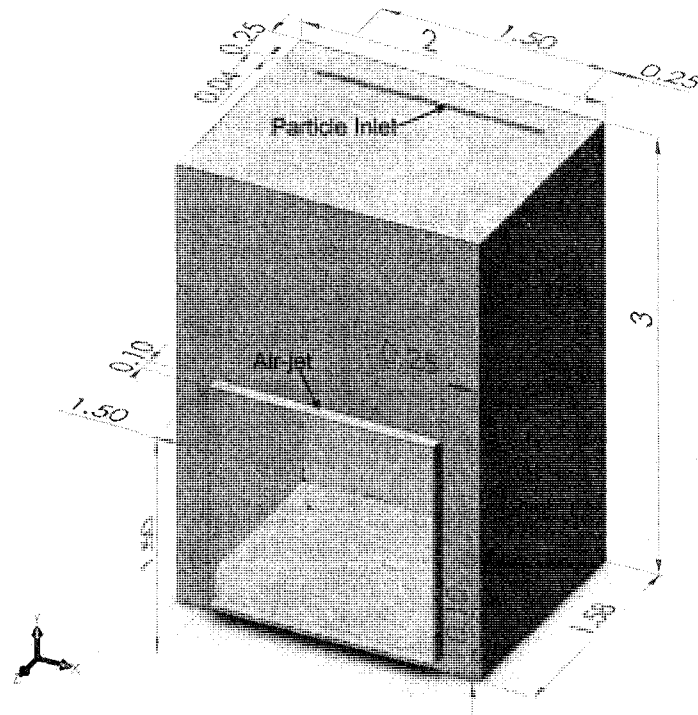


Figure 2.5 Conceptual design of the SPSR for the computational fluid dynamics (CFD) study (unit: m)

CHAPTER 3

NUMERICAL METHOD AND ALGORITHM

This chapter introduces the numerical methods and algorithm that are used in evaluating the performance of the solid particle solar receiver with the influence of an air-jet. Assumptions and system working boundary conditions are described, and the governing equations and simulation models are introduced in this chapter.

In this research, a two-way coupled Euler-Lagrange method is implemented. The momentum and heat transfer between the particles and gas are considered. The governing equations used to express gas-solid thermal aerodynamics are solved in the Cartesian coordinate system with a control-volume finite difference method which is introduced by Patankar [36]. The commercial software Fluent is used to simulate the performance of solid particle solar receiver.

3.1 Numerical Model Assumptions

Several assumptions in the numerical model are made to investigate the performance of SPSR. For the simplicity of describing SPSR, a few assumptions may be too ideal, but they provide a good standard to analyze the important factors which influence performance. Numerical model assumptions are listed below.

1. Solar flux is in the direction normal to the front open aperture with a fixed value.

2. The size of the particles is assumed to be the same, and with the same spherical shape.
3. Air is assumed to be incompressible and follow the ideal gas law.
4. The particle properties are constant, no agglomeration occurs and no fracture in high temperature occurs.
5. The environmental influence on the SPSR like wind, temperature and humidity are ignored in this study.
6. The wall of SPSR is assumed to be adiabatic.

3.2 Governing Equations and Numerical Model

3.2.1 Air Flow Equation

Inside the SPSR, falling particles can achieve a very high temperature by absorbing radiation heat energy. At the same time, the air surrounding the falling particles is also heated up to form a complicated gas-solid flow pattern, which contains rotation and recirculation. The Reynolds number can reach 1.6×10^5 in this problem. As this is a typical turbulent flow, the velocities and temperatures items in the calculation equations contain a mean and a fluctuating part, $u_j = U_j + u'_j$ for velocity and $T = \bar{T} + T'$ for temperature. The time-averaged partial differential governing equations for describing the gas phase mass, momentum, and energy can be expressed as:

Continuity:

$$\frac{\partial \rho U_j}{\partial x_j} = 0 \quad (3.1)$$

Mómentum equation:

$$\frac{\partial}{\partial x_j}(\rho U_i U_j) = -\frac{\partial P}{\partial x_i} + \frac{\partial}{\partial x_j} \left[\mu \left(\frac{\partial U_i}{\partial x_j} + \frac{\partial U_j}{\partial x_i} \right) - \rho \overline{u_i u_j} \right] + S_i^M - \rho g_i \quad (3.2)$$

Here ρ is the density, μ is the viscosity, P is the pressure, and S_i^M is the momentum per unit volume added to the gas flow by the influence of particles. The turbulence stress is described as:

$$\rho \overline{u_i u_j} = \frac{2}{3} \rho \delta_{ij} k - \mu_T \left(\frac{\partial U_i}{\partial x_j} + \frac{\partial U_j}{\partial x_i} \right) \quad (3.3)$$

$\mu_T = \rho C_\mu k^2 / \varepsilon$ is the turbulence viscosity, where $C_\mu = 0.09$ and ε is the turbulence dissipation. And k is the kinetic energy, δ_{ij} is the Kronecker delta function, $\delta_{ij} = 1$ when $i = j$ and zero when $i \neq j$.

Energy equation:

$$\frac{\partial}{\partial x_j}(\rho U_j C_p T) = \frac{\partial}{\partial x_j} \left(\alpha \frac{\partial T}{\partial x_j} - \rho C_p \overline{u_j T} \right) + S_i^T \quad (3.4)$$

$$\rho C_p \overline{u_j T} = -\frac{\mu_T}{Pr_t} \frac{\partial T}{\partial x_j} \quad (3.5)$$

Where C_p is the specific heat capacity, α is the thermal conductivity, S_i^T is the energy per unit volume added to the gas phase by the influence of particles. Pr_t is the turbulent Prandtl number and defined as 0.9.

3.2.2 Turbulence Model

Fluctuations in the transport quantities such as momentum, energy, and species are the characteristics labeled by the turbulence flow. These kinds of fluctuation can be small or large depending on the description of practical use in the simulation calculation. It is well known that no single turbulence model is universally acceptable for all classes

of problems. So the selection of the turbulence model largely depends on consideration of the physics properties in a specific problem. In Fluent, there are several selections for the turbulence model, and the purpose of this section is to analyze the computational efforts, cost in terms of CPU time and memory, and also the appropriation of describing the flow on the selection of realizable $\kappa - \varepsilon$ turbulence model in this problem.

Different methods of calculating the turbulence flow have been proposed in the literature review research in Chapter 1. And the $\kappa - \varepsilon$ turbulence model is presently the most widely used and validated of the two-equation models. It is determined from the solution of transport equations for the turbulence kinetic energy and the energy dissipation rate, and produces a relatively satisfactory result for the results of complex flows. This technique is available for the wall functions to treat the near-wall sub-layers. The realizable $\kappa - \varepsilon$ model [28] is a relatively recent turbulence model. The term “realizable” means that the model is consistent with the physics of turbulence flows and satisfies certain mathematical constraints. Neither the standard $\kappa - \varepsilon$ model nor the RNG $\kappa - \varepsilon$ model is realizable. Compared with them, the realizable $\kappa - \varepsilon$ model provides superior performance for flows involving rotation, boundary layers under strong adverse pressure gradients, recirculation, and separation. It also has the immediate benefit of predicting the spreading rate of both planar and round jets more accurately [37]. Finally, the performance of realizable $\kappa - \varepsilon$ model has been found to be substantially better than that of the other models.

In the realizable $\kappa - \varepsilon$ model, a new realizable eddy viscosity formulation and a new transport equation for the dissipation rate ε are derived from an exact equation. The eddy viscosity is no longer constant in the realizable $\kappa - \varepsilon$ model, and it relies on the

mean strain and rotation rates, the turbulence fields, and the angular velocity of the system rotation. The modeled transport equations for κ and ε in the realizable $\kappa-\varepsilon$ model are expressed as follow:

$$\frac{\partial}{\partial x_j}(\rho k U_j) = \frac{\partial}{\partial x_j} \left[\left(\mu + \frac{\mu_T}{\sigma_\varepsilon} \right) \frac{\partial k}{\partial x_j} \right] + G_k + G_b - \rho \varepsilon \quad (3.6)$$

$$\frac{\partial}{\partial x_j}(\rho \varepsilon U_j) = \frac{\partial}{\partial x_j} \left[\left(\mu + \frac{\mu_T}{\sigma_\varepsilon} \right) \frac{\partial \varepsilon}{\partial x_j} \right] + \rho C_1 S_\varepsilon - \rho C_2 \frac{\varepsilon^2}{k + \sqrt{\nu \varepsilon}} \quad (3.7)$$

In these equations, G_k represents the generation of turbulence kinetic energy due to the mean velocity gradients, $G_k = -\rho \overline{u_i' u_j'} \frac{\partial u_j}{\partial x_i}$. G_b is the generation of turbulence kinetic energy due to buoyancy, calculated as: $G_b = -g_i \frac{\mu_t}{\rho \text{Pr}_t} \frac{\partial \rho}{\partial x_i}$. Here $C_1 = \max \left[0.43, \frac{\xi}{\xi + 5} \right]$, $\xi = S \frac{k}{\varepsilon}$, $S = \sqrt{2 S_{ij} S_{ij}}$ is the modulus of the mean rate strain tensor, and $C_2 = 1.9$. The terms σ_k and σ_ε are the turbulent Prandtl numbers for κ and ε , $\sigma_k = 1.0$, $\sigma_\varepsilon = 1.2$. The inlet boundary condition of κ and ε depend on the turbulence intensity I , turbulence length scale l and the inlet velocity, expressed as:

$$\kappa = \frac{3}{2} (u \cdot I)^2 \quad (3.8)$$

$$\varepsilon = \frac{C_\mu^{3/4} k^{3/2}}{l} \quad (3.9)$$

Here $I = 0.16 \text{Re}^{-1/8}$ and $l = 0.07 D_h$, Re is the Reynolds number based on the length of the top inlet. In this research configuration, the turbulent intensity is 5%. The hydraulic diameter D_h is 0.1 m.

3.2.3 Equations of Particles

As mentioned in Chapter 1, the numerical model uses a two-way coupled Euler-Lagrange method. The trajectories of the particles are predicted by integrating the force balance in the Lagrange reference frame. So the force balance which equals the particle inertia force with the force acting on the solid particle can be written as:

$$\frac{du_{p,i}}{dt} = \frac{18\mu}{\rho_p d_p^2} \frac{C_D \text{Re}_{p,i}}{24} (u_i - u_{p,i}) + \frac{g_i(\rho_p - \rho)}{\rho_p} \quad (3.10)$$

where $u_{p,i}$, ρ_p , and d_p are the velocity, density and diameter of the particle, respectively.

$\text{Re}_{p,i}$, the relative Reynolds number, can be written as:

$$\text{Re}_{p,i} = \frac{\rho d_p |u_{p,i} - u|}{\mu} \quad (3.11)$$

and C_D , the drag force coefficient, can be expressed as:

$$C_D = \frac{24}{\text{Re}_{p,i}} (1 + 0.15 \text{Re}_{p,i}^{2/3}) \quad (3.12)$$

In this case, $\text{Re}_{p,i}$ is up to 10^3 , so the drag coefficient can be expressed above by the method introduced by Clift et al. [38]. Because the material and gas density ratio is very large, the effect of the pressure gradient and particle acceleration on drag coefficient can be neglected. Here, the particle volume fraction is very small and the diameter of the particle is much smaller than the distance between particles, so the particle-particle drag influence and collision can be neglected during the calculation.

The energy equation for the particle is given as:

$$\frac{\rho_p C_p \pi d_p^3}{6} \frac{dT_p}{dt} = Nu \alpha_p \pi d_p (T - T_p) + \pi d_p^2 \varepsilon_p \sigma (T_R^4 - T_p^4) \quad (3.13)$$

where the Nu is the Nusselt number defined by

$$Nu = 2 + 0.6 Re_p^{1/2} Pr^{1/3} \quad (3.14)$$

here Pr is the Prandtl number of the gas flow, ε_p is the particle emissivity, σ is the Stefan-Boltzman constant, α_p is the thermal constant of the particle, and T_r is the radiation temperature, which is determined by :

$$T_r = (G / 4\sigma)^{1/4} \quad (3.15)$$

here G is the incident radiation value,

$$G = \int_{\Omega=4\pi} I d\Omega \quad (3.16)$$

3.2.4 Radiation Model

The radiation model used in this study considered the interaction between the radiation field and the falling particle curtain. To keep the accuracy of the calculation, a discrete ordinate (DO) method with a solar ray tracing model is used inside the solar receiver. The DO radiation model solves the radiative transfer equation for a finite number of discrete solid angles, each of them associated with a direction noted by \vec{s} in the global Cartesian coordinate. The DO model solves for as many transport equations as there are directions \vec{s} . The radiative transfer equation can be written as:

$$\nabla \cdot (I_\lambda(\vec{r}, \vec{s}) \vec{s}) + (a_\lambda + \sigma_s) I_\lambda(\vec{r}, \vec{s}) = a_\lambda n^2 I_{b\lambda} + \frac{\sigma_s}{4\pi} \int_0^{4\pi} I_\lambda(\vec{r}, \vec{s}') \Phi(\vec{s} \cdot \vec{s}') d\Omega' \quad (3.17)$$

$I_\lambda(\vec{r}, \vec{s})$ is the spectral intensity in direction \vec{s} and position \vec{r} of an absorbing, emitting, and scattering medium. λ is the wavelength, a_λ is the spectral absorption coefficient, σ_s is the scattering coefficient, \vec{s}' is the scattering direction vector, Φ is phase function, Ω' represents solid angle, and $I_{b\lambda}$ is the black body intensity given by the Planck

function. The total intensity is computed as $I(\vec{r}, \vec{s}) = \sum_k I_{\lambda_k}(\vec{r}, \vec{s}) \Delta\lambda_k$, where the summation is over the wavelength bands.

The solar ray tracing algorithm can be used to predict the direct illumination source which results from the direct solar incidence. It takes a beam that modeled the position of the sun vector and illumination parameters, applies it to any wall or inlet/outlet boundary conditions, and performs a face-by-face shading analysis to determine well-defined shadows on all boundaries.

3.2.5 User Defined Function on the Drag Force

In the discrete phase model, particles interact with a continuous phase. A user defined function on the drag force is applied on each particle to evaluate the particle behavior under the influence of heat buoyancy force and gravity force balance.

3.3 Numerical Modeling Approach

A three-dimensional model of the solid particle solar receiver (SPSR) with the influence of an air-jet is analyzed. The free-falling down particles will form a solid particle curtain and be directly heated by the reflected solar energy that passes through the aperture of the cavity. The mass, momentum and energy exchange between the solid particle phase and gas fluid phase are simulated by the two-way coupling Euler-Lagrange method. A discrete ordinate radiative transfer method has been applied to study the coupling of radiative heat transfer and the falling particle curtain. The realizable $\kappa - \varepsilon$ model is used in the investigation of turbulence flow. In order to predict the performance of the SPSR, the aerodynamic behavior of the particles and thermal interaction, which include particle-particle radiation, particle-wall radiation, particle-air

convection, and air-wall convection are analyzed and demonstrated in this work. The numerical results of the parametric studies will be discussed in Chapter 4 and Chapter 5.

3.4 Solution Algorithm

3.4.1 Pressure-Velocity Coupling: SIMPLE

FLUENT provides several kinds of pressure-velocity coupled methods. For this problem, increasing the pressure-correction under-relaxation to 1.0 can lead to instability, because of the huge grid size. Under this situation, a slightly conservative under-relaxation is needed, and a selection of SIMPLE algorithm is necessary. The acronym SIMPLE stands for Semi-Implicit Method for Pressure-Linked Equations. This algorithm is essentially a guess-and-correct procedure for the calculation of pressure on the staggered grid [23].

3.4.2 Second-Order Upwind Scheme

A volume discretization scheme stores discrete values of the scalar and values at faces must be interpolated from the cell center value. This is accomplished by using an upwind scheme. Upwind means that the value at interface is derived from the data in upstream cells. There are several upwind schemes, and a second-order upwind scheme is applied in this problem. In this scheme quantities at the cell face are computed using a multidimensional linear reconstruction approach [39]. Higher-order accuracy is achieved at the cell interface through the Taylor series expansion of the cell-centered solution. Second-order upwind is available in the pressure-based and density-based solvers.

3.4.3 PRESTO Scheme

The PRESTO (pressure staggering option) scheme is the discretization scheme for the pressure in flows with high swirl number, high-Rayleigh-number natural convection, and high-speed rotating.

3.4.4 Under-relaxation Factors

Under-relaxation factors contain the factors for all equations in the pressure-based solver. It includes turbulence variables and viscosities, which are solved separately in all equations. In the beginning, the under-relaxation parameters are set to be default values for calculation. In this complicated natural convection problem the density is strongly coupled with temperature, so the under-relaxation factors can be adjusted under default values to achieve convergent results.

3.5 Boundary Conditions

Before the solid particles fall down from the top opening of the cavity, along each trajectory, the particles have an initial temperature of 873 K, and are given an initial falling speed of 0.088 m/s. A two-band isotropic radiation calculation is made with a solar band from 0.2 to 1.5 micron and an infrared band from 1.5 to 30 micron. An incident solar flux of 920 suns is applied through the open aperture of the cavity.

3.5.1 Pressure Outlet Boundary Condition

Pressure outlet boundary conditions require the specification of a static pressure at the outlet boundary. The boundary containing the area around the SPSR is set as pressure outlet boundary. A set of “backflow” conditions are specified, because reverse flow should occur at the exit during the calculation. At the pressure outlet, a constant zero gauge pressure is entered, with a total backflow temperature of 300 K. In order to

determine the direction of the backflow, the direction of the flow in the cell layer adjacent to the pressure outlet is selected.

3.5.2 Velocity Inlet Boundary Condition

As mentioned earlier, the air-jet has the potential of decreasing the convection and radiation loss from the SPSR. So the velocity inlet boundary condition is applied in the air-jet, which is on top of the receiver aperture. The velocity inlet boundary condition is used to define the flow velocity, along with all other relevant scalar properties of the flow. This kind of boundary is intended to be used in incompressible flow. In this research, a velocity specification method defined the magnitude and the direction of the air-jet.

3.5.3 Wall Boundary Condition

Wall boundary conditions are used to bound gas and particle flow in this study. Since the flow is modeled as viscous flow, the no-slip boundary condition is enforced at the wall. The heat flux is assumed to be zero (i.e. adiabatic) in the present research. The wall of the cavity with an internal emissivity of 0.8 and absorptivity of 0.9 are used for both bands (visible and infrared). The bottom wall can trap the falling particles, while the side walls reflect the particles striking on them.

3.6 Physical Properties Used in the Numerical Model

The detailed information related to the physical prosperities of the solid particles and gas flows in the numerical model are listed in Table 3.1.

Table 3.1 Operating conditions of gas flow and physical properties of the solid particle

Gas Flows	Solid Particle
Inlet Air Temperature of air-jet: 300-700 K	Particle Density: 3200 kg/m ³
Operating Pressure: 101000 Pa	Heat Capacity: 1085 J/kg-K
Incompressible Ideal Gas	Thermal Conductivity: 6.67 W/m-K
	Particle Diameter: 60- 800 micron

3.7 Mesh Independent Study

In this research, GAMBIT is used as a pre-processor to create a computational mesh. Several computational meshes have been generated to check the grid independence. Meshes with 197,892, 332,960, 533,400, 717,094, and 909,441 cells have been investigated. Figure 3.1 gives the positions of the lines and points, along which data are plotted and compared. Figure 3.2 shows the velocity distribution along line 1 (x=1 m, y=1.4 m, z=0 m) to (x=1 m, y=1.4 m, z=1.58 m) and Figure 3.3 shows the velocity distribution along line 2 (x=0 m, y=0.7 m, Z=0.8 m) to (x=2 m, y=0.7 m, z=0.8 m). Both figures present very uniform velocity distribution tendency and magnitudes, except for the mesh with smallest cell number.

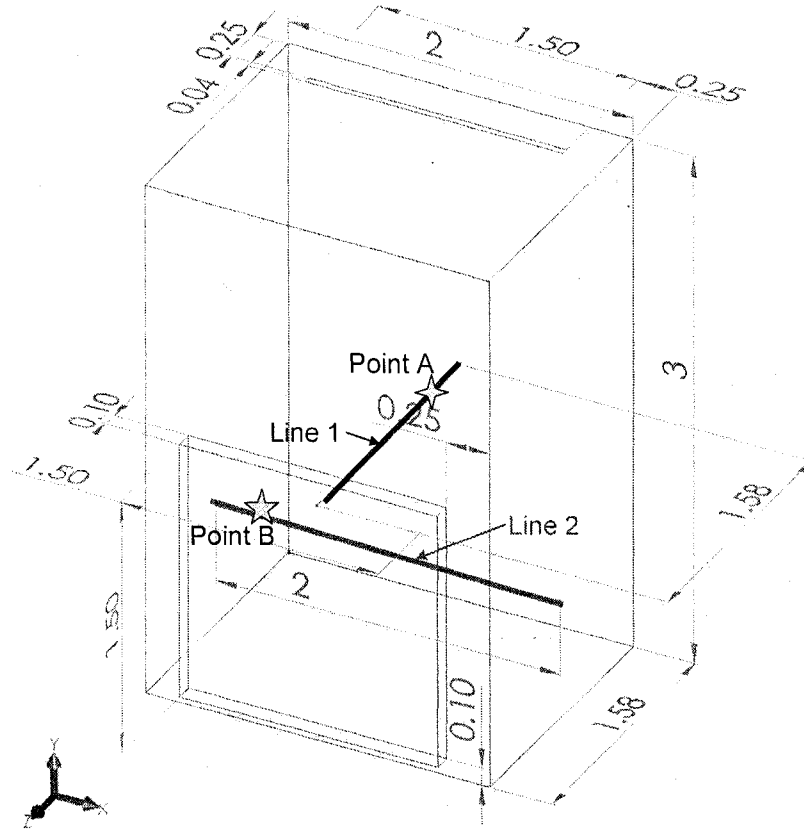


Figure 3.1 The positions of line 1 and line 2, point A and point B

Figure 3.4 and Figure 3.5 show the velocity relative error percentages at point A ($x=1$ m, $y=1.4$ m, $z=0.3$ m) and point B ($x=0.15$ m, $y=0.7$ m, $z=0.8$ m). The results conclude that the mesh with 533,400 cells, as shown in Figure 3.6, has velocity relative error percentages under 10 % for both the point value, compared with the finest mesh. To save the computational resources and time, a computational mesh with 533,400 cells is used in the continuing research work.

Refined and gradient mesh is designed in the boundary, open aperture and particle curtain region of the SPSR, as shown in Figure 3.7. This can provide an accurate result for the place that has larger pressure, temperature and velocity differences.

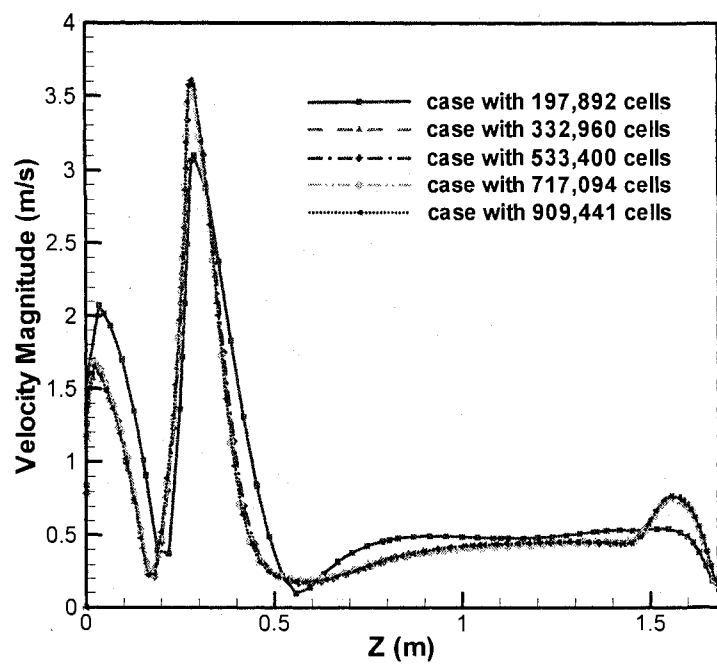


Figure 3.2 Velocity magnitude along line 1

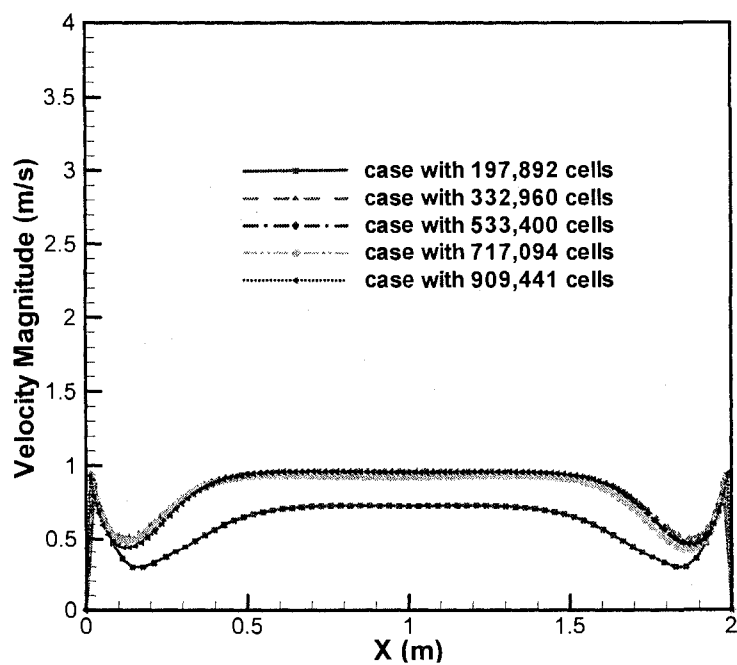


Figure 3.3 Velocity magnitude along line 2

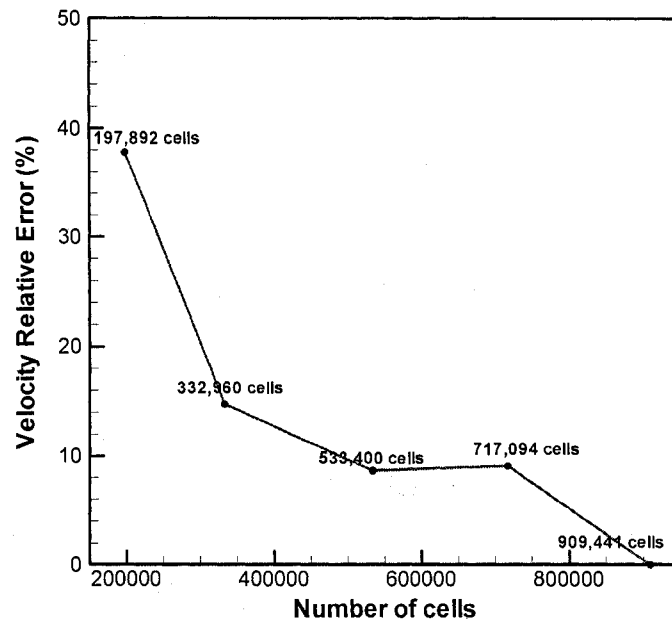


Figure 3.4 Velocity relative error compares to the finest mesh at point A

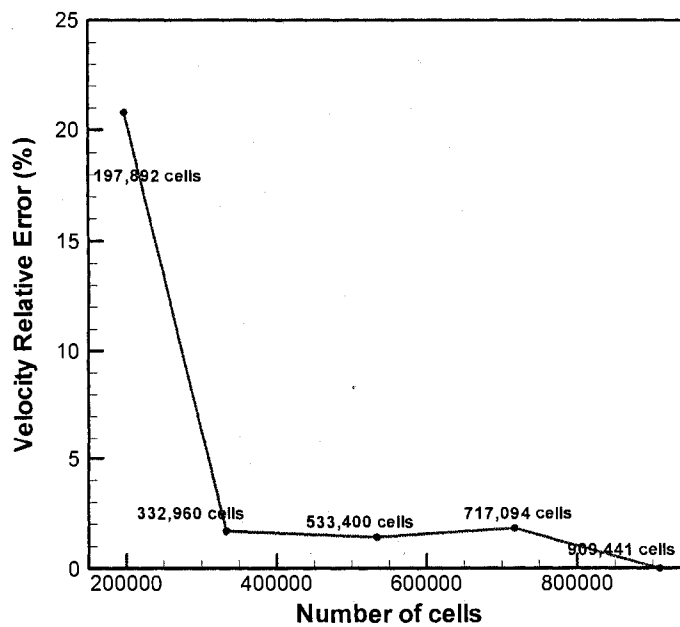


Figure 3.5 Velocity relative error compares to the finest mesh at point B

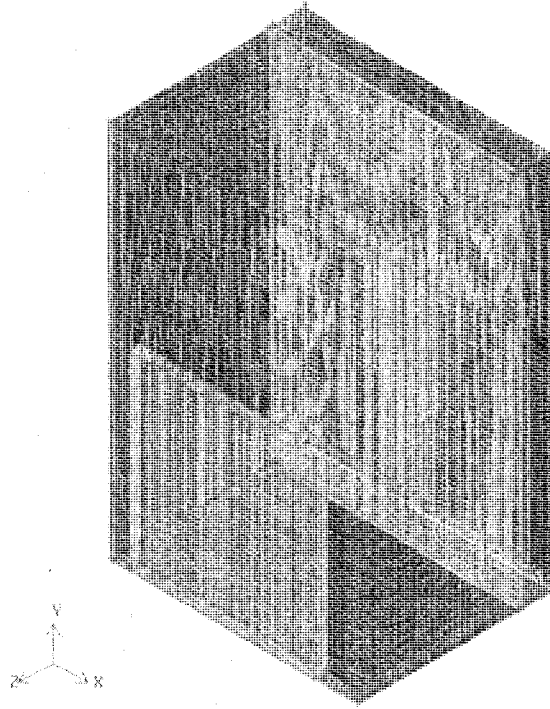


Figure 3.6 Computational mesh of the SPSR

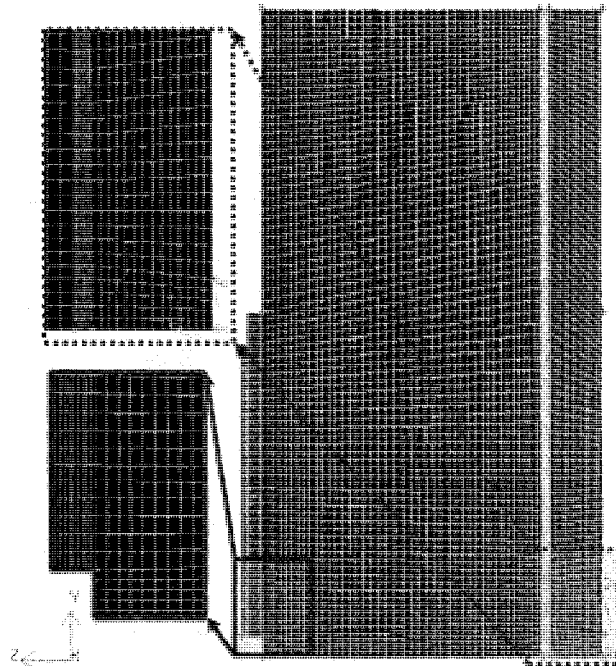


Figure 3.7 Computational mesh of the SPSR viewed from Y-Z coordinates

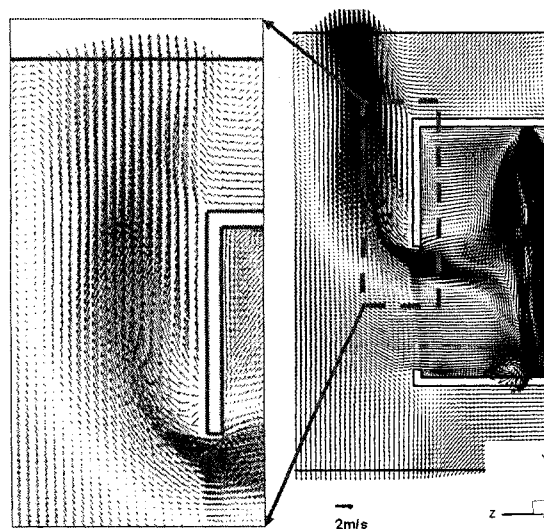
CHAPTER 4

NUMERICAL SIMULATION OF A THREE-DIMENSIONAL SOLID PARTICLE SOLAR RECEIVER

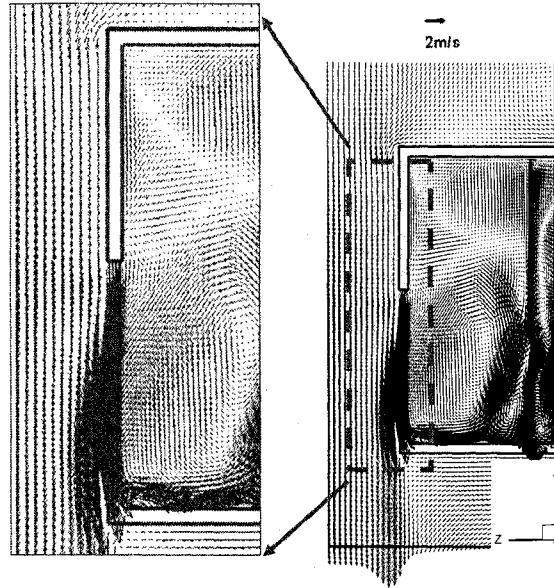
Numerical modeling of the SPSR was done by SNL more than 20 years ago. All the parametric studies which are based on the two-dimensional design do not consider the influence of an air-jet. Three-dimensional computational fluid dynamics studies of the SPSR were first studied by Chen et al. [30], to compare cavity efficiency and average exit particle temperature with and without bottom opening. And the influence of air-jet on SPSR was studied by Tan et al. [40] and Chen et al. [41]. The effect of an air-jet has been studied and proved to reduce the convection loss of a central solar receiver, by isolating the interior from the surrounding environment [9]. In this solid particle solar receiver study, the air-jet has the additional benefit of protecting the spreading of the solid particles, which are light and could leak to the outside with heat energy. In a practical design, the SPSR will be set up on a very high solar tower, where the wind from different directions in that elevation can blow the heat media solid particles out of the receiver, if there is no protection. The characteristics of the air-jet based on the conceptual design can be investigated by performing parametric studies related to the cavity efficiency and the exit particle temperature. The results can provide the fundamental engineering information for the solid particle solar receiver scale-up design.

4.1 Comparison of SPSR with and without an Air-jet

Typical air flow patterns with and without an air-jet in the selected slice ($x=1$ m, center plane of the receiver) are shown in Figure 4.1. Here, particle diameter is chosen as 650 micron, particle initial temperature is given as 873 K, particle mass flow rate is 5 kg/s, and particle initial downward speed is 0.088 m/s. A uniform solar incident radiation flux of 920 suns is considered in front of the solid particle curtain. Both the particles and the back wall are heated by the solar radiation. As a result, a buoyancy force is generated around the particle curtain. There is a strong air circulating occurring in the region between the front aperture and particle curtain, as shown in Figure 4.1 (a). A large amount of air is entering into the cavity through the bottom of the aperture from outside. As the temperature of the air entering into the receiver through the aperture is much lower than that inside the receiver, the cavity efficiency and exit particle temperature will be reduced due to the energy loss by convection.



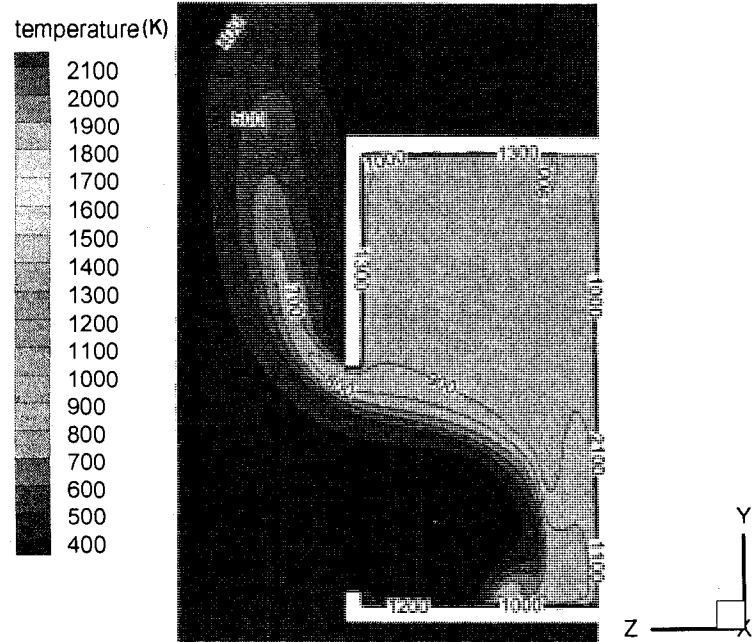
(a) Without an air-jet



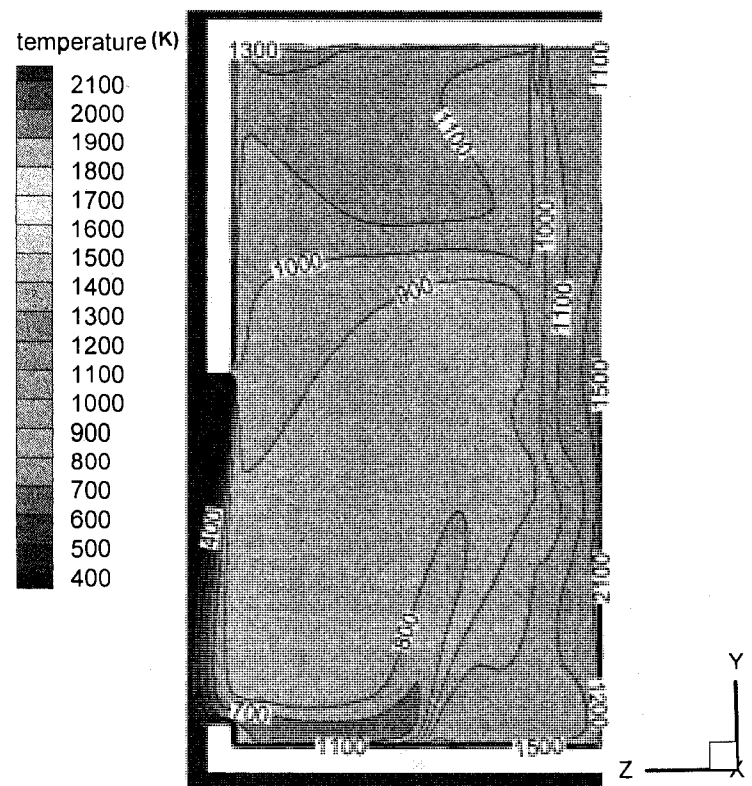
(b) Air-jet velocity is 8 m/s

Figure 4.1 Air flow pattern without an air-jet (a) and with an air-jet (b)

Figure 4.1 (b) illustrates the effect of applying an air-jet to cover the open aperture. There still exists a strong clockwise circulation between the aperture and particle curtain. But the injected downwards air-jet wind blocks this circulation from moving outwards. Small air exchanges between the cavity and outside field can happen by convection. This is the expected air flow pattern for SPSR designers. Figure 4.2 shows the temperature (K) contours at slice $x = 1$ m (in the centerline of the receiver). Both designs can reach the highest temperature of 2100 K at the back walls by absorbing the incident solar flux. But temperature inside the receiver is reduced in Figure 4.2 (a) by sucking cold air flow from outside. For the case with protection from an air-jet, as shown in Figure 4.2 (b), the air temperature inside cavity can keep a relatively high value.



(a) Without an air-jet



(b) Air-jet velocity is 8 m/s

Figure 4.2 Temperature (K) contours without an air-jet (a) and with an air-jet (b)

The thermal performances of the SPSR are characterized by the cavity efficiency and average exit particle temperature. The cavity efficiency is introduced as:

$$\eta = \frac{Q_p}{Q_{inc}} \quad (4.1)$$

Where Q_p is the absorption energy gain of the solid particles, and Q_{inc} is the total incident solar energy that comes through the aperture. Obviously, the total incident solar energy value is constant if the solar incident flux doesn't change. The radiation loss percentage is defined as the ratio of radiation heat loss $Q_{radloss}$ and total incident solar energy Q_{inc} , the same as convection heat loss percentage, which is defined as the ratio of convection heat loss $Q_{cnvloss}$ and total incident solar energy Q_{inc} .

Table 4.1 compares the cavity efficiencies, average exit particle temperatures, heat convection and radiation loss percentages with and without air-jet. It clearly shows the performance improvement of SPSR after applying an air-jet.

Table 4.1 Cavity efficiencies, average exit particle temperatures, heat convection and radiation loss percentages with and without an air-jet

	η	T_{p-exit} (K)	$\frac{Q_{radloss}}{Q_{inc}}$	$\frac{Q_{cnvloss}}{Q_{inc}}$
Without Air-jet	0.51	1066	0.3	0.17
With Air-jet	0.62	1108	0.3	0.05

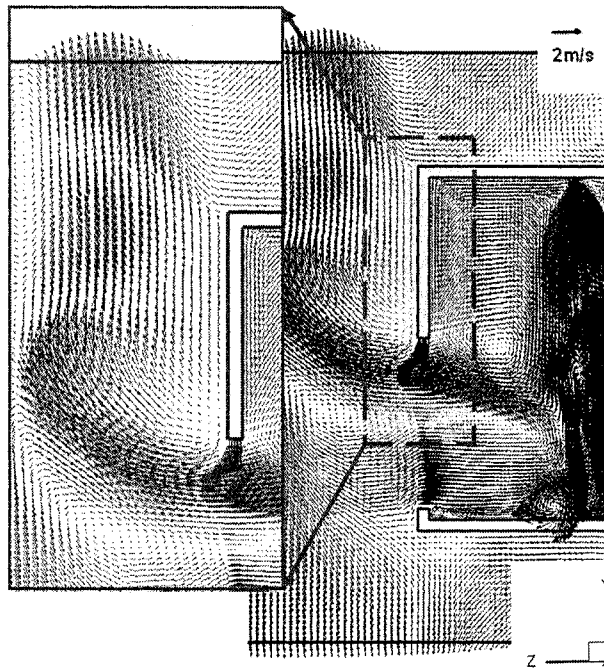
4.2 Parametric Studies of SPSR

In section 4.1, comparisons of the SPSR with and without air-jet are made to evaluate the benefit of an air-jet. But the designs of an air-jet, like air-jet velocity and air-jet temperature, have not been considered. In this part, several parametric studies are performed to identify the optimized operating conditions for SPSR.

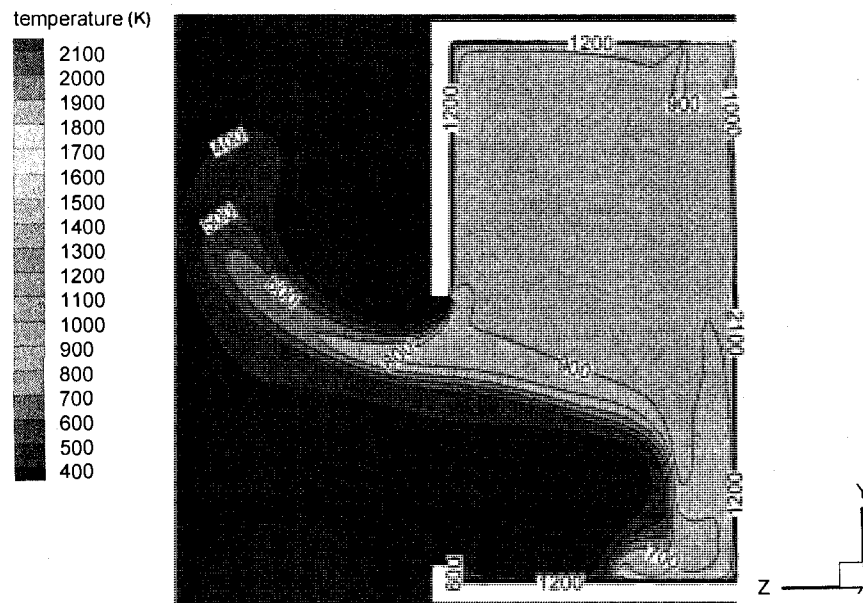
4.2.1 Aerodynamic Analysis of SPSR with Different Air-jet Velocities

The SPSR with an air-jet of 8 m/s performs better than the one without an air-jet, as shown in section 4.1. A range of 0 m/s – 10 m/s air-jet velocities are numerically tested to find the optimized velocity result in this numerical model, with all the same working conditions of SPSR except air-jet velocity. Mass flow rate is 5 kg/s, downward air-jet temperature is 300 K, mass flow rate is 5 kg/s, and solar flux value is 920 suns. From Figure 4.3 to Figure 4.6, including Figure 4.1 and Figure 4.2, all the air flow patterns and temperature contours at the central plane of the receiver give a very reasonable explanation of the result that is concluded in Figure 4.7. In Figure 4.7, the cavity efficiencies and average exit particle temperatures keep on increasing from air-jet velocity of 0 m/s upto 8 m/s. For the cases of air-jet velocity magnitudes less than 8 m/s, the air flow patterns show that air-jets are not powerful enough to cover the whole aperture. But as the air-jet velocity increases, much more heated air is protected inside the cavity. The temperature contours also show the air encirclement tendency inside the cavity. From Figure 4.7, air-jet velocity of 8 m/s provides a good screening result, better than 10 m/s. In this investigation of optimal working velocity, each air-jet has an initial temperature of 300 K, which is lower than the air temperature inside the cavity. When velocity of an air-jet reaches a high value, it might blow the cold wind of the air-jet into

the cavity. This explains that selection of 10 m/s air-jet is not necessary in this numerical model, even through it covers the whole aperture as shown in Figure 4.6.

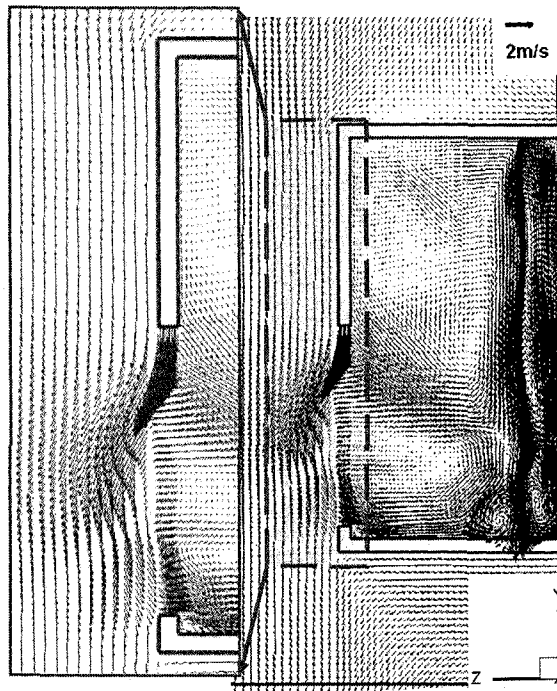


(a) Air flow pattern

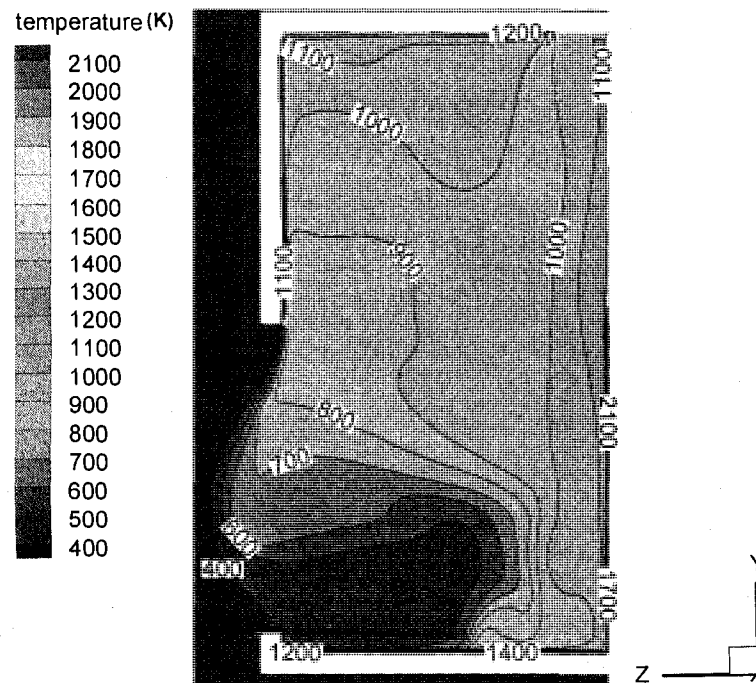


(b) Temperature contours (K)

Figure 4.3 Air flow pattern (a) and temperature contours (b) at slice $x = 1$ m. Air-jet velocity is 2 m/s.

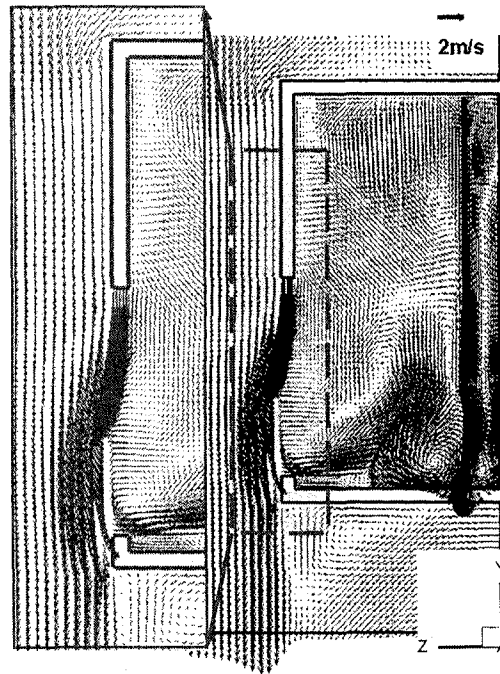


(a) Air flow pattern

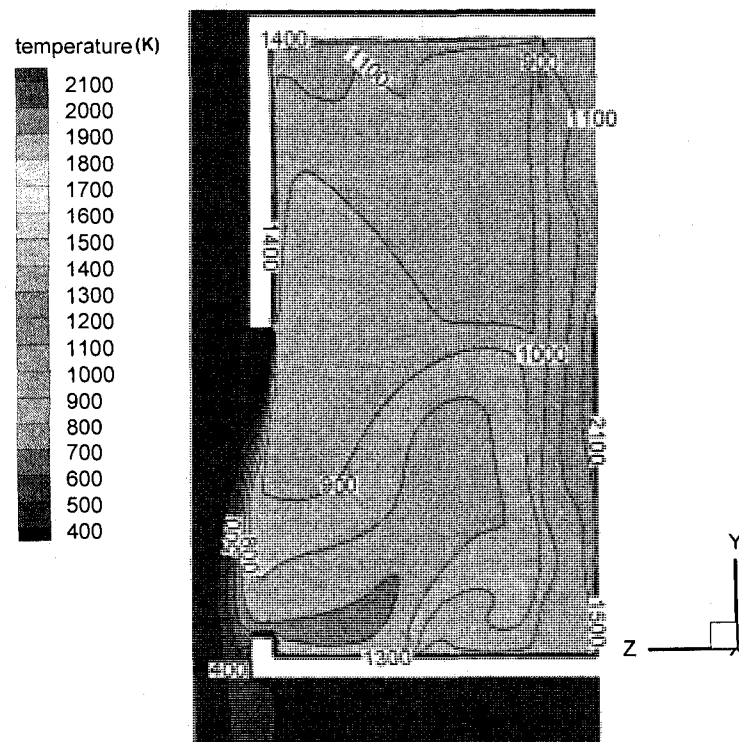


(b) Temperature contours (K)

Figure 4.4 Air flow pattern (a) and temperature contours (b) at slice $x=1$ m. Air-jet velocity is 4 m/s.

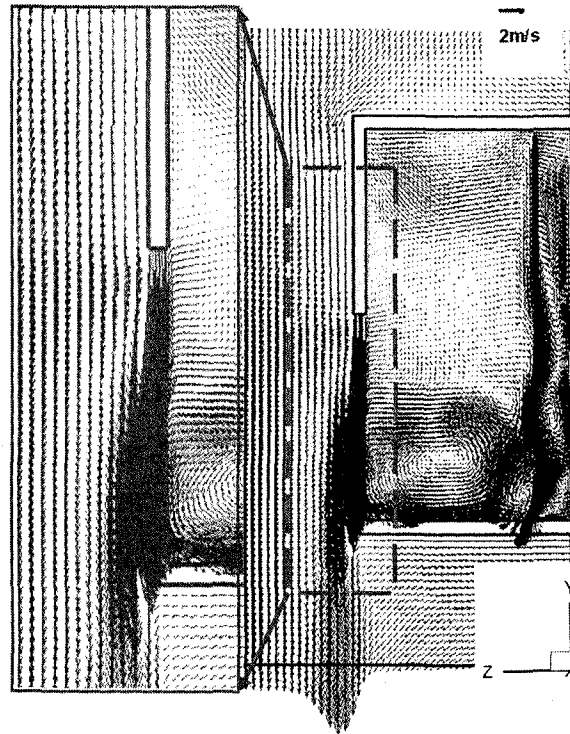


(a) Air flow pattern

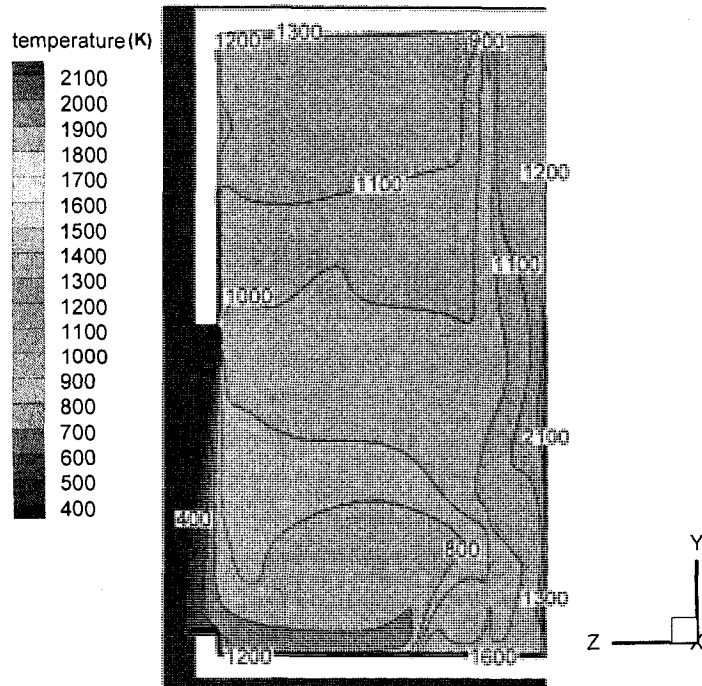


(b) Temperature contours (K)

Figure 4.5 Air flow pattern (a) and temperature contours (b) at slice $x=1$ m. Air-jet velocity is 6 m/s.



(a) Air flow pattern



(b) Temperature contours (K)

Figure 4.6 Air flow pattern (a) and temperature contours (b) at slice $x=1$ m. Air-jet velocity is 10 m/s.

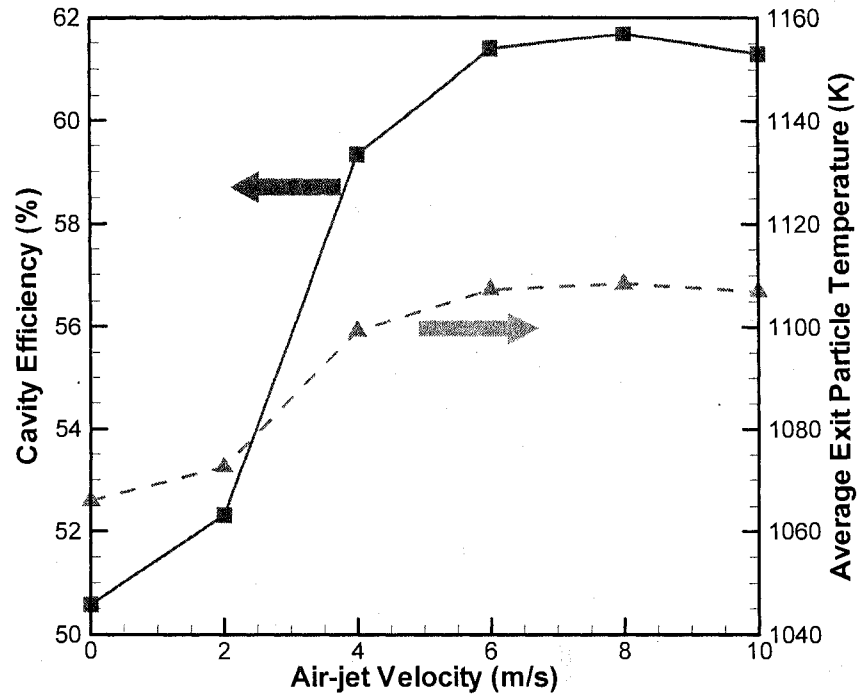


Figure 4.7 Cavity efficiencies of SPSR and average exit particle temperatures as a function of different air-jet velocities

Figure 4.8 shows the radiation loss and convection loss percentages as a function of different air-jet velocities. The radiation loss percentage value is almost constant in the tested air-jet velocity range of 0 m/s – 10 m/s, which occupies about 30 % of the total incident solar energy. The convection loss percentage keeps on decreasing until the air-jet velocity reaches 8 m/s, which is the smallest value of convection loss and also gives the best performance of SPSR in the tested velocity range. These phenomena prove that an air-jet is capable of reducing convection heat loss.

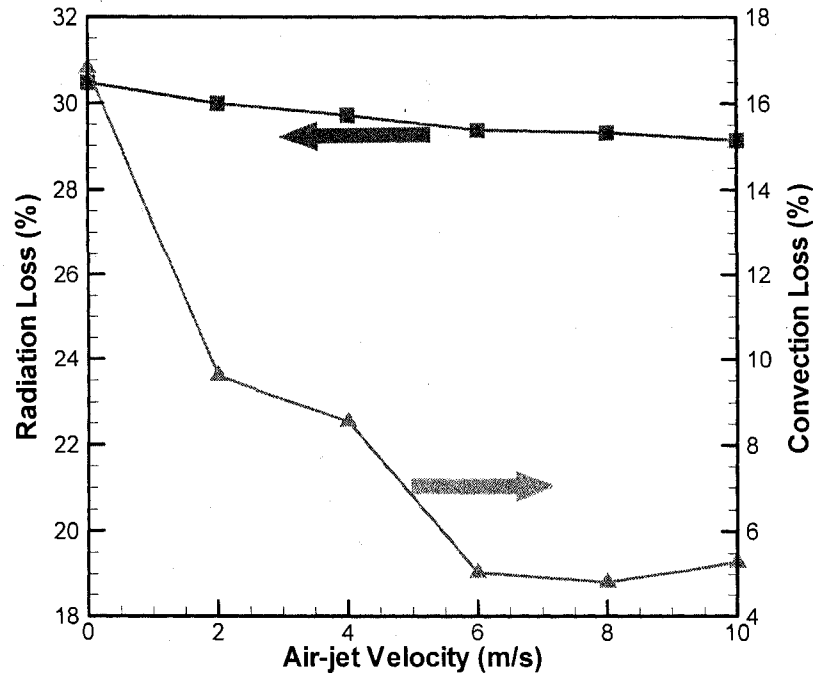


Figure 4.8 Radiation loss and convection loss percentages as a function of different air-jet velocities

4.2.2 The Influence of Different Air-jet Temperatures on SPSR

Since a temperature of 300 K is a low initial value for an air-jet, it may inject this cold air into the SPSR. An assumption of increasing initial temperature of an air-jet to obtain a better performance of the SPSR is made. To save the energy cost for running the air-jet, the pre-heat air, which exists around high temperature particles, can be recuperated. Through this method, the initial temperature of the air-jet can reach about 700 K. Other working conditions are the same: the downward air-jet velocity is 8 m/s, particle diameter is 650 micron, mass flow rate is 5 kg/s, and solar flux value is 920 suns. To characterize the air flow clearly, the air flow stream lines, which are released from the air-jet, are shown in Figure 4.9. In this case the air-jet velocity is 8 m/s, and the initial temperature is 700 K. The stream lines with high temperature are pushed forwards, and

cause a leakage in the bottom of the aperture. Cold air from surroundings is drawn into the cavity of the SPSR. This figure also shows air flow pattern and temperature contours in the centerline of the receiver, which demonstrate the backflow of cold air clearly. The air-jet stream lines in Figure 4.10, which has the same air-jet velocity but with an initial temperature of 300 K, shows that the air curtain injected by the air-jet is able to seal the open aperture. As a result, the increased temperature of the air-jet can not reach a better performance than the one of low temperature. The pre-heat air from the air-jet causes a buoyancy force, which forms a strong backflow of air and pushes the air stream lines from the air-jet away from the aperture. If the temperature of the air-jet is not as high as 700 K, the buoyancy force may not be that strong. The result of air-jet with lower temperature is shown in Figure 4.11, but there still exists leakage. The air-jet velocity of 8 m/s may be not strong enough to balance that buoyancy force. Figure 4.12 shows stream lines of a stronger air-jet flow, where the velocity is 10 m/s and the temperature is 700K. No great improvement of the performance has been found through this design.

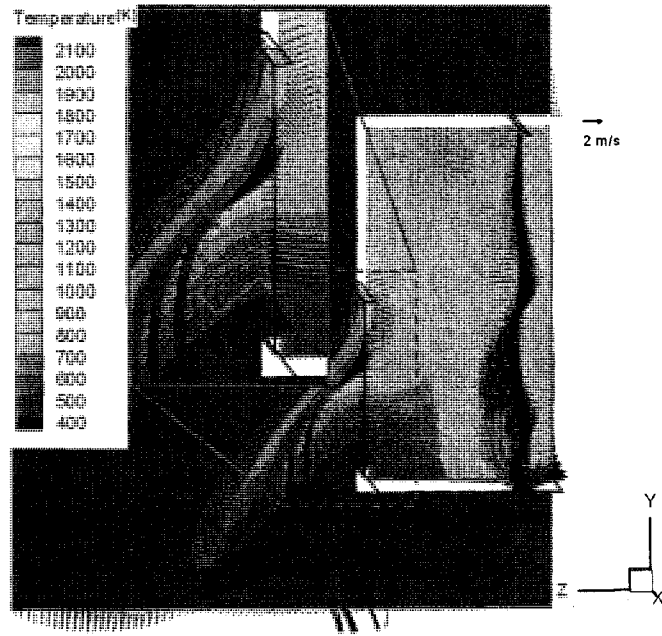


Figure 4.9 Air flow stream lines released from air-jet. The stream line is colored by temperature. Air-jet velocity is 8 m/s and air-jet temperature is 700 K.

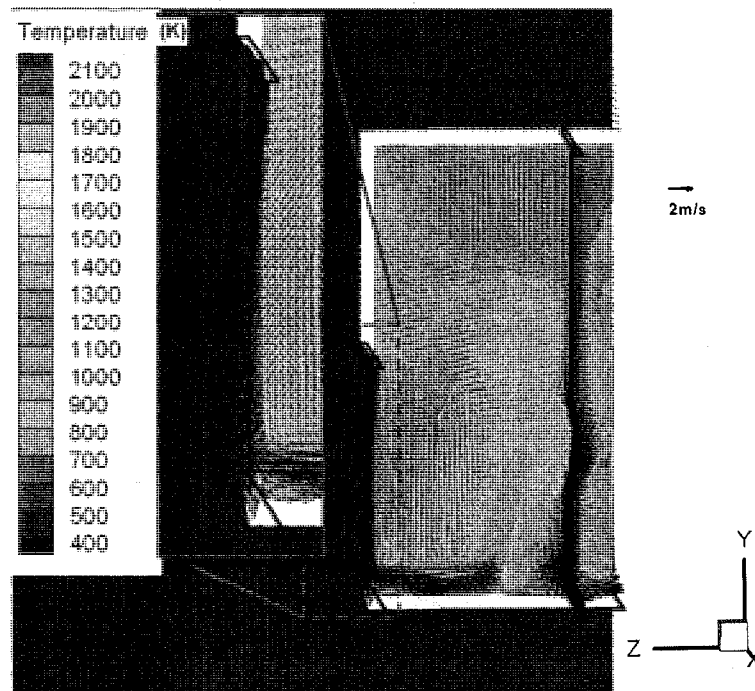


Figure 4.10 Air flow stream lines released from air-jet. The stream line is colored by temperature. Air-jet velocity is 8 m/s and air-jet temperature is 300 K.

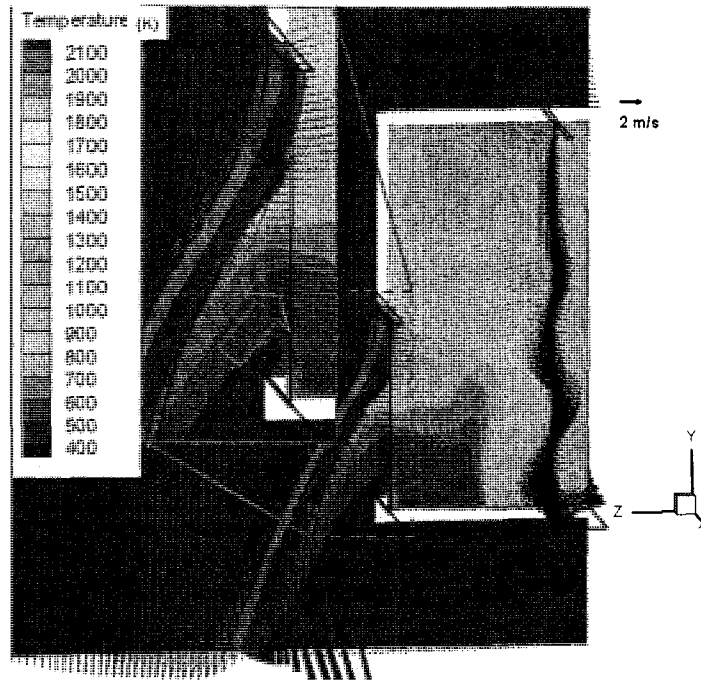


Figure 4.11 Air flow stream lines released from air-jet. The stream line is colored by temperature. Air-jet velocity is 8 m/s and air-jet temperature is 500 K.

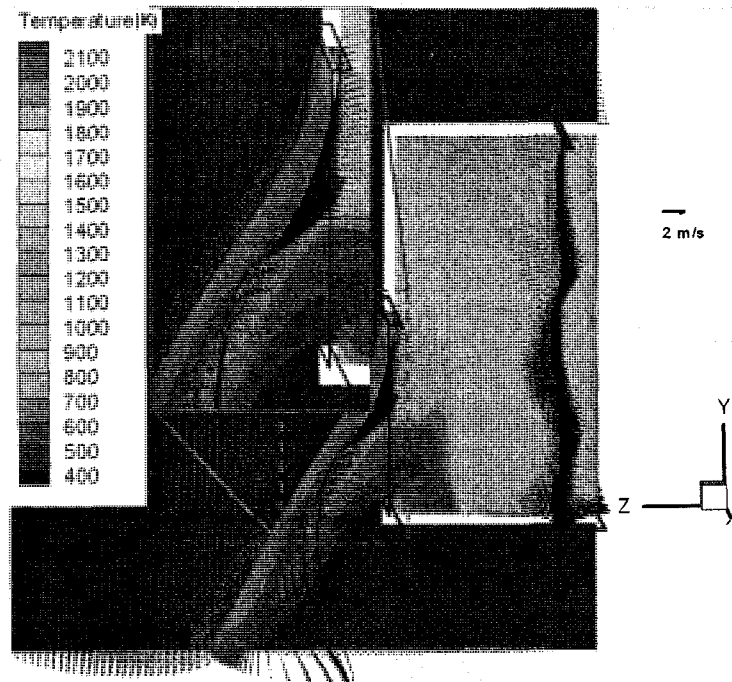


Figure 4.12 Air flow stream lines released from air-jet. The stream line is colored by temperature. Air-jet velocity is 10 m/s and air-jet temperature is 700 K.

Table 4.2 summarizes the performance of the SPSR with air-jet temperature in the range of 300 K to 700 K, and a velocity range of 6 m/s to 10 m/s. All results don't show big differences, so the different temperatures application of a downward air-jet won't influence the performance of the SPSR.

Table 4.2 Cavity efficiencies and average exit particle temperatures with different air-jet velocities and different air-jet temperatures

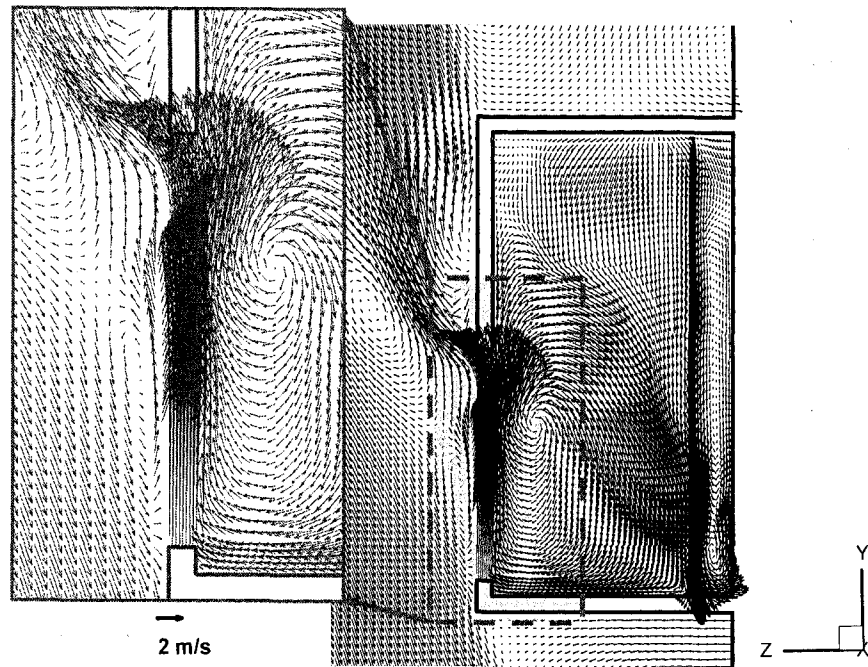
Velocity of Air-jet (m/s) Temperature of Air-jet (K)	6		8		10	
	η	T_{P-exit} (K)	η	T_{P-exit} (K)	η	T_{P-exit} (K)
300	0.61	1107	0.62	1108	0.61	1106
500	0.61	1105	0.60	1104	0.62	1111
700	0.60	1100	0.61	1105	0.61	1106

4.2.3 Air-jet Injected from the Bottom of Open Aperture

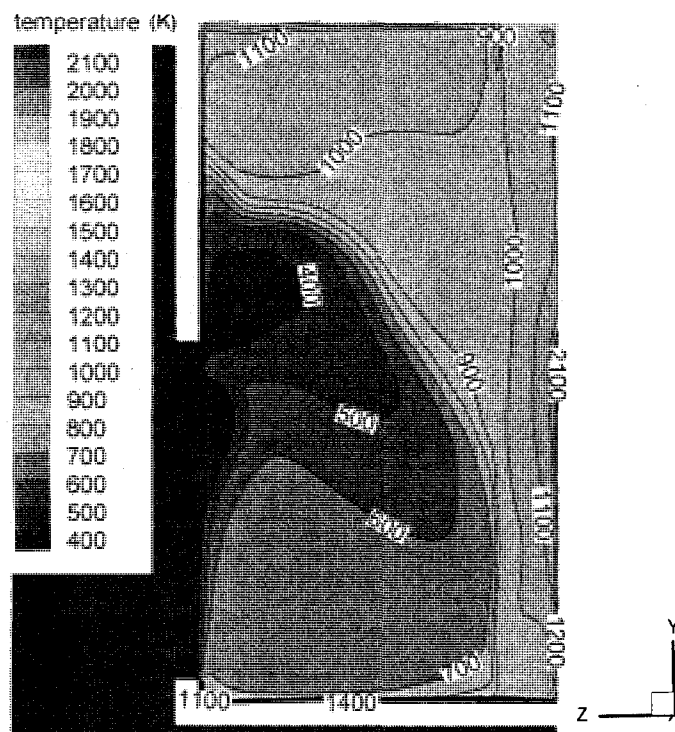
A model of applying a downward pre-heated air-jet to cover the open aperture is proved to be useless on improving the performance of the SPSR. A buoyancy force is generated by temperature differences between the air-jet and surrounding area, which pushes the air-jet forward and causes leakage. An air-jet injected upward from the bottom of the aperture is investigated, such that a buoyancy force can act in the same direction as the air flow of the air-jet. From the air flow pattern of the air-jet without being heated, as shown in Figure 4.13 (a), the air from the air-jet blows into the cavity, distorts the flow to lower the cavity efficiency. From Figure 4.13 (b), the temperature contour describes the

400 K isotherm inside cavity, which well demonstrates the invasion of cold air. Under this situation, the cavity efficiency is $\eta = 60\%$, and average exit particle temperature is $T_{p-exit} = 1102K$. This case showed the air flow behavior without considering the heat buoyancy force.

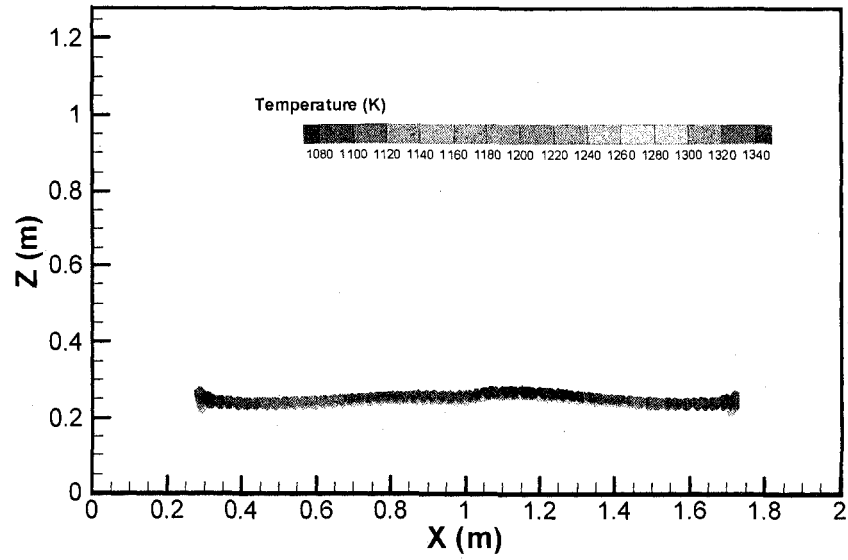
The same model with initial air-jet temperature of 700 K is studied, and this temperature of air-jet is much higher than the surrounding temperature of 300 K. As a result, a floating force is created to hold the injection direction of air-jet. From Figure 4.14 (a), the air flow pattern illustrates the well formed air-jet curtain, which protects the heat inside the cavity. Even air from air-jet injects into the cavity, which is shown from the 700 K isotherm in Figure 4.14 (b), this high value of temperature cannot influence the performance inside the cavity. Here, cavity efficiency increases to $\eta = 62\%$, and average exit particle temperature is 1110 K. From Figure 4.13 (c) and Figure 4.14 (c), the particle distributions on the bottom plane appear to be steady and uniform. Compared to the performance of air-jet injected from top, preheat air-jet injected from bottom of open aperture doesn't improve much on the performance of SPSR.



(a) Air flow pattern at slice $x=1$ m

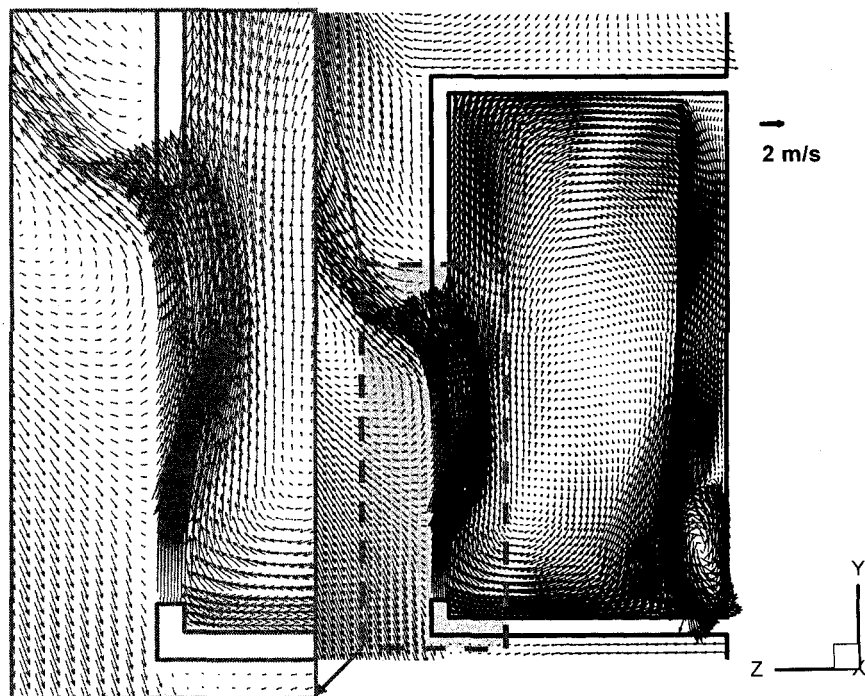


(b) Temperature contour at slice $x=1$ m

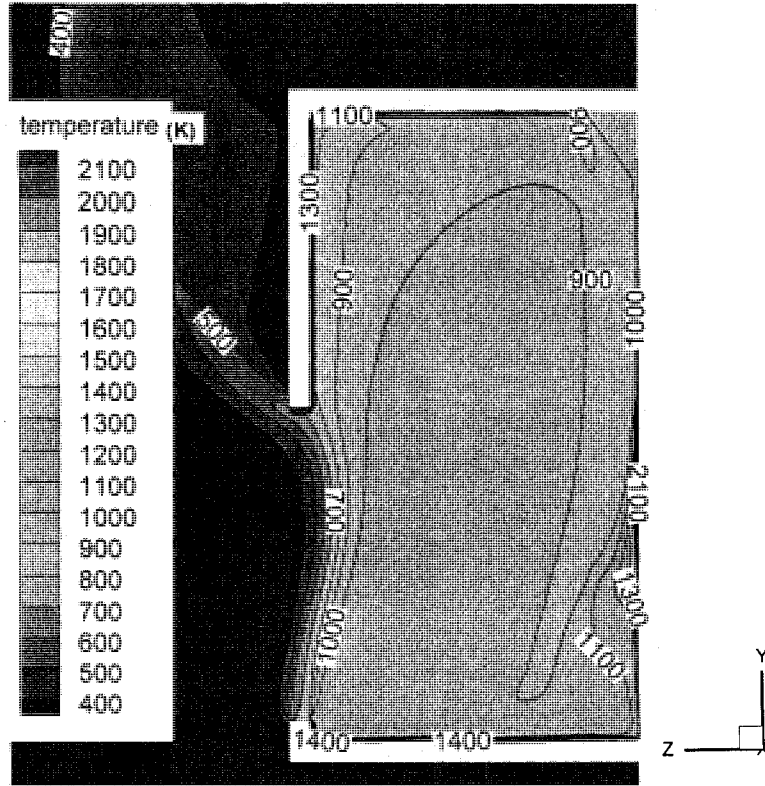


(c) Particle distributions on the bottom plane, colored by temperature (K)

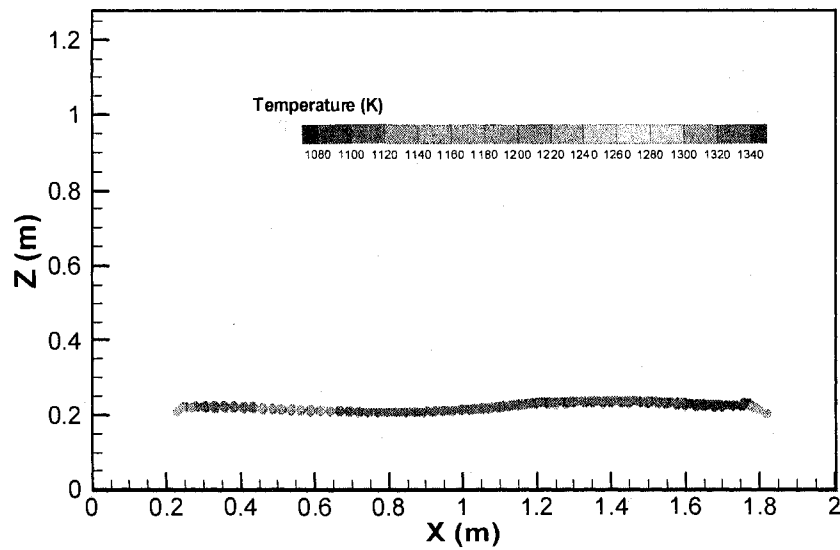
Figure 4.13 Air-jet injected from bottom of aperture. The velocity of air-jet is 8 m/s, temperature is 300 K, mass flow rate is 5 kg/s, diameter of particle is 650 micron, and solar flux is 920 suns



(a) Air flow pattern at slice $x=1$ m



(b) Temperature contour at slice $x=1$ m



(c) Particle distributions on the bottom plane, colored by temperature (K)

Figure 4.14 Air-jet injected from bottom of aperture. The velocity of air-jet is 8 m/s, and temperature is 700 K, mass flow rate is 5 kg/s, diameter of particle is 650 micron, and solar flux is 920 suns

4.2.4 The Influence of Different Particle Diameters on SPSR

Chen et al. [30] show the heated particle curtain with smaller diameter does not remain as flat as the larger ones, and is more capable of reaching higher temperature. Hruby's [32] research results also conclude that smaller particle size can bring both higher efficiency and exit temperature. The present study considers the influence of an air-jet. Cavity efficiency and average exit particle temperature relate to the characteristics of the solid particles. The trajectory of the solid particle is predicted by integrating the force balance on the particle. The force balance on each particle equals the particle inertia force with the force acting on each particle. Buoyancy force acts more predominantly on particles with smaller diameter than larger ones, which helps smaller particles to stay in the cavity for a longer time, and accept more solar irradiation. Based on the model of a two-way coupled Euler-Lagrange method, the calculation includes the exchange of heat and momentum between the gas phase and particles. But it neglects the effect of the nearby particles on the drag force. This assumption is reasonable when the particle volume fraction is very small and the particle distance is much larger than the diameter of the particles. From Figure 4.15 and Figure 4.16, the particle volume fraction at the center slice ($x=1\text{m}$) of the cavity shows that the particle fractions are small enough to neglect the particle-particle force at different heights.

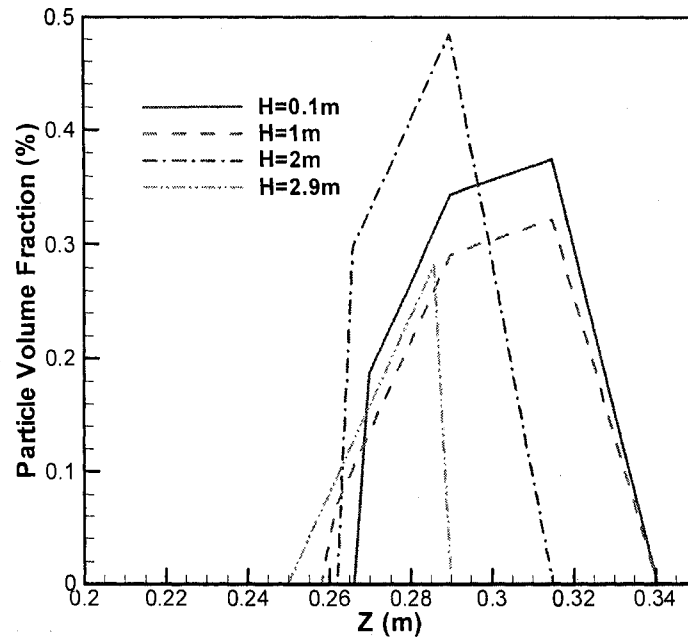


Figure 4.15 Particle volume fraction as a function of distance from back wall at different height in select slice ($x=1\text{ m}$). The diameter of the particles are 200 micron, and air-jet velocity is 8m/s. H is the distance from the bottom wall.

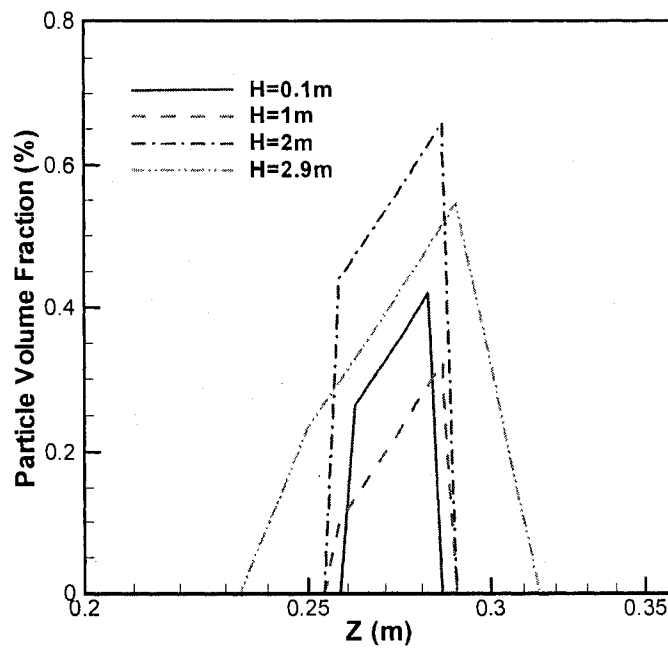


Figure 4.16 Particle volume fraction as a function of distance from back wall at different height in select slice ($x=1\text{ m}$). The diameter of the particles are 650 micron, and air-jet velocity is 8m/s. H is the distance from the bottom wall.

Figure 4.17 gives the result of the SPSR cavity efficiency and average exit particle temperature as a function of different particle diameters with an air-jet velocity of 8m/s. Applying a smaller particle size in the SPSR shows a higher average exit particle temperature, resulting in higher cavity efficiencies. The smaller particles might spread due to strong turbulence air flow pattern inside the cavity, which will cause particle and energy loss. From the particle volume fraction figures, this possibility can be neglected. Most of the particles stay to form a relatively uniform curtain without any particle mass loss, until the diameter of particles decreases to 60 microns, which is too small to stay inside the cavity, and particles start to leak from the front aperture. So theoretically, the particle with diameter in the range of 70-80 micron gives the best performance of SPSR. And the cavity efficiency begins to decrease when the diameter is less than 70 micron, because of the heat energy carried away by the leaking particles. On the other hand, particles that keep inside cavity still increase their average exit temperature, because of the longer residence time.

Figure 4.18 and Figure 4.19 show the particle distributions on the bottom plane in the cases of particle diameter 200 micron and 650 micron, colored by the temperature. 700 particles are tracked on each calculation step, so the particles with different size appear the same number on the bottom. Over time, the solid particle diameter of 200 micron case will have more particles falling to the bottom. The particle distributions on the bottom show the curtains have not been pushing towards the front or back of the cavity, which means the air-jet is very effective at protecting the particle flow inside cavity. From the particle distribution colored by temperature, the smaller particle size of 200 micron case reaches higher average exit temperature.

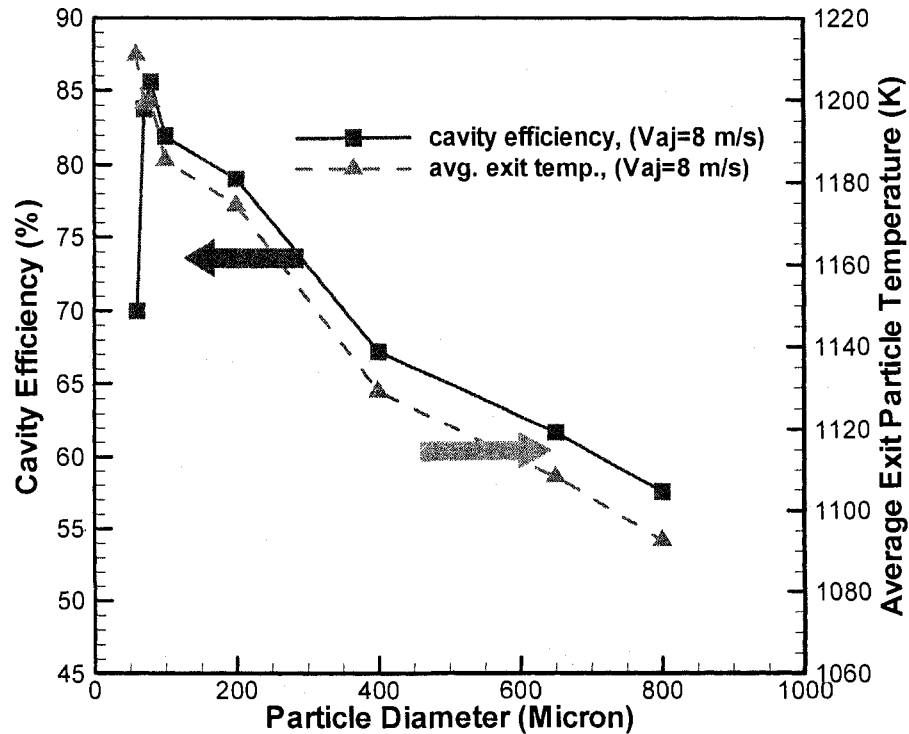


Figure 4.17 Cavity efficiency and average exit particle temperature as a function of particle diameters, velocity of air-jet is 8 m/s, downward air-jet temperature is 300 K, mass flow rate is 5 kg/s, and solar flux is 920 suns

Previous analysis concludes that smaller particle size can bring higher cavity efficiency and average exit particle temperature. Theoretically, the optimized size of the solid particle is 70-80 micron, and particles with diameter less than this range will spread out of the cavity. This proves the existence of a limitation on the size of the particle, because small particles will spread, and distort the particle curtain. The simulation analysis provides the optimized SPSR working condition on the particle size, but this ideal small particle size might be unpractical for manufacture, and cause agglomeration

and fracture under extremely high temperature, which largely depends on the characteristics of the particle material.

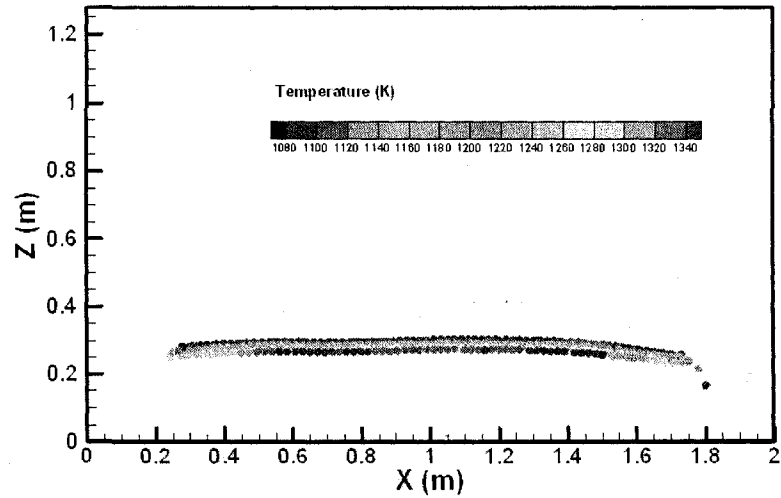


Figure 4.18 Particle distributions on the bottom plane. Particle size is 200 micron, and air-jet velocity is 8 m/s.

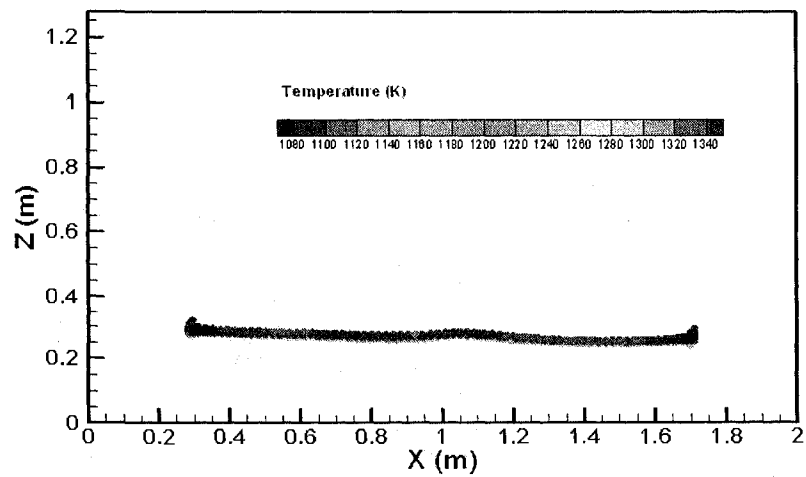


Figure 4. 19 Particle distributions on the bottom plane. Particle size is 650 micron, and air-jet velocity is 8 m/s.

Figure 4.20 is the particle distributions on the bottom plane, colored by temperature with the particle diameter of 100 micron. Compared to the case of 200 micron and 650 micron, the distribution pattern turns out to be a curve that is pushed to the back of the wall. The track of the particle on the bottom is distributed more widely, and with a relatively uniform temperature. Several particles are attracted to the wall. This phenomenon has been found by using 100 micron diameter of the particle. It is because the back flow drag-force and buoyancy force hold the particle inside the cavity for a longer time and some particles cannot hold the starting falling projection position when they fall to the bottom.

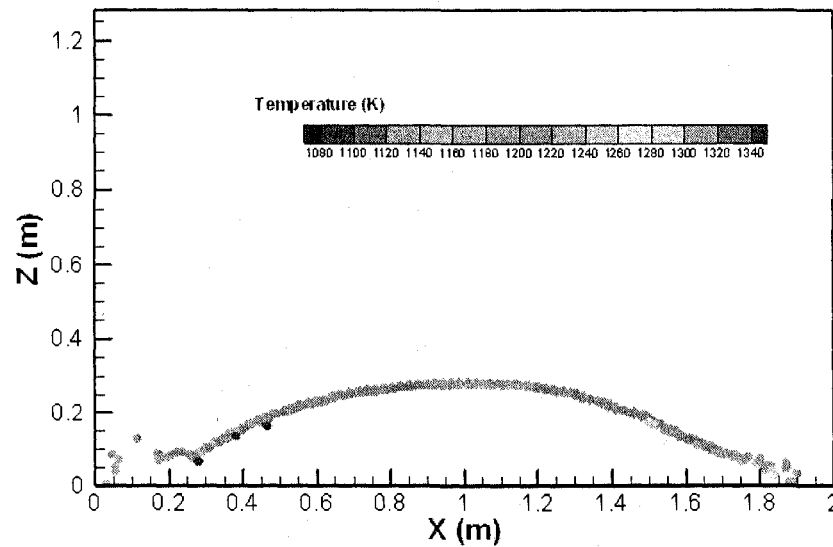


Figure 4. 20 Particle distributions on the bottom plane. Particle diameter is 100 micron, and air-jet velocity is 8 m/s

Higher cavity efficiency and average exit particle temperature of the SPSR is achievable by decreasing the diameter of solid particles. While the size of particle is too small, it is unable to stay inside the cavity under the influence of strong buoyancy force. And leakage of high temperature particles will cause thermal energy loss. So it is necessary to find out the optimized range of particle size, which not only brings the highest average exit particle temperature but also keeps all the particles inside the cavity. Figure 4.21 and Figure 4.22 show the particle distribution on the bottom plane when the diameter of the solid particles decreases to 80 and 70 micron. And other working conditions of the SPSR are the same as previous cases with larger size of solid particles. The downward air-jet velocity is 8 m/s, air-jet temperature is 300 K, mass flow rate is 5 kg/s, and solar flux value is 920 suns. At these conditions, the particles still stay inside the cavity with a better performance compared to larger size of the solid particles. Figure 4.23 is the particle distribution on the bottom plane with a diameter of 60 micron, and it shows the spreading of particles. It is been told that the cavity efficiency starts to decrease when the diameter of solid particles is less than 70 micron, because the heated particles start to leak out of the cavity from the aperture, and this causes heat energy loss. On the other hand, the average exit particle temperature of SPSR with particle diameter of 60 micron is still increasing. This result just calculates the temperature of the solid particles that are trapped on the bottom plane and does not consider the other leaking particles. Each trapped small particle can absorb more heat energy, compared to larger size of solid particles.

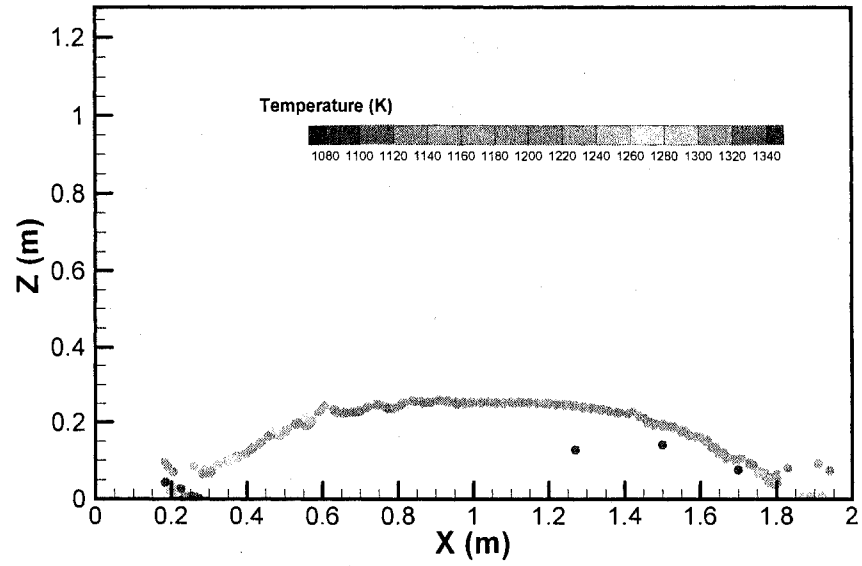


Figure 4. 21 Particle distributions on the bottom plane. Particle diameter is 80 micron, and air-jet velocity is 8 m/s

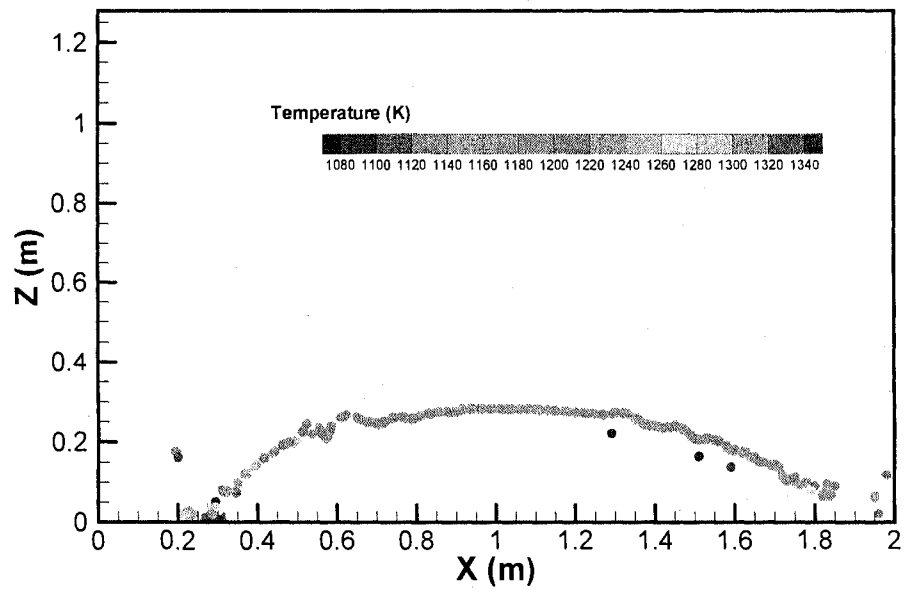


Figure 4. 22 Particle distributions on the bottom plane. Particle diameter is 70 micron, and air-jet velocity is 8 m/s

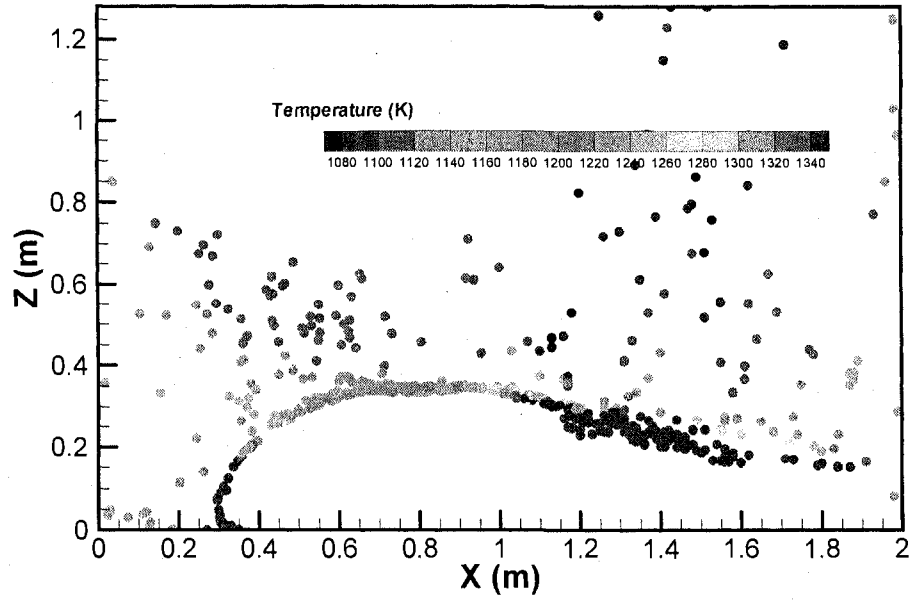


Figure 4. 23 Particle distributions on the bottom plane. Particle diameter is 60 micron, and air-jet velocity is 8 m/s

4.2.5 Aerodynamic Analysis of SPSR with Different Particle Mass Flow Rates

The control of mass flow rates can be realized by adjusting the opening size of the particle inlet. And the volume percentage of particle inside the cavity is still under 1 % assumption when the mass flow rate is 7 kg/s. It promises there is no particle-particle collision in this mass flow rate calculation range. So the simulation model is acceptable. Figure 4.24 demonstrates that increasing particle mass flow rate leads to increased cavity efficiency and decreased average exit particle temperature. Larger mass flow rates can bring more particles to transport absorbed solar energy, which will increase the overall efficiency. On the other hand, more particles will increase the thickness and reduce the transparency of particle curtain, which prevents some particles from absorbing the radiated and reflected energy, resulting in a decreased average exit particle temperature.

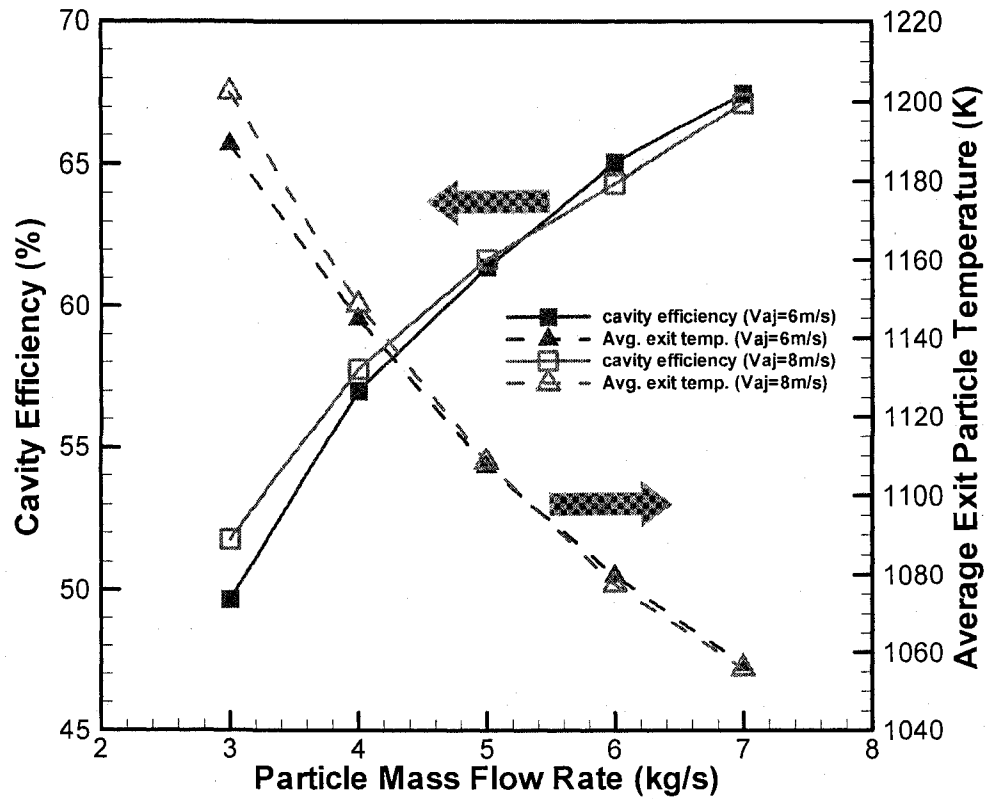


Figure 4. 24 Cavity efficiency and average exit particle temperature as a function of different particle mass flow rates, downward air-jet temperature is 300 K, mass flow rate is 5 kg/s, diameter of particles is 650 micron, and solar flux is 920 suns

4.2.6 The Influence of Different Solar Irradiation Values on SPSR

The solar irradiation intensity is another important input to the simulation. It will be varied depending on different latitudes, longitudes, and elevations around the earth. Even in the same location, different season and time during each day will get different results. The base modeling case uses the solar irradiation value of 920 suns. The parametric study focused on solar flux will provide important information for the time and location operation instructions on the SPSR. Figure 4.25 shows the changing tendency of the efficiency and exit temperature with 650 suns, 920 suns, and 1280 suns

solar fluxes with the influence of air-jet velocities 6 m/s and 8 m/s. The intensified irradiation will obviously bring higher cavity efficiency and average exit particle temperature. And in an intensified irradiation working condition, the SPSR with an air-jet velocity of 6 m/s performs more effectively than air-jet velocity of 8 m/s, which means that the heat convection loss is higher in SPSR with an air-jet velocity of 8 m/s. This is because stronger air-jet winds blow in cold air.

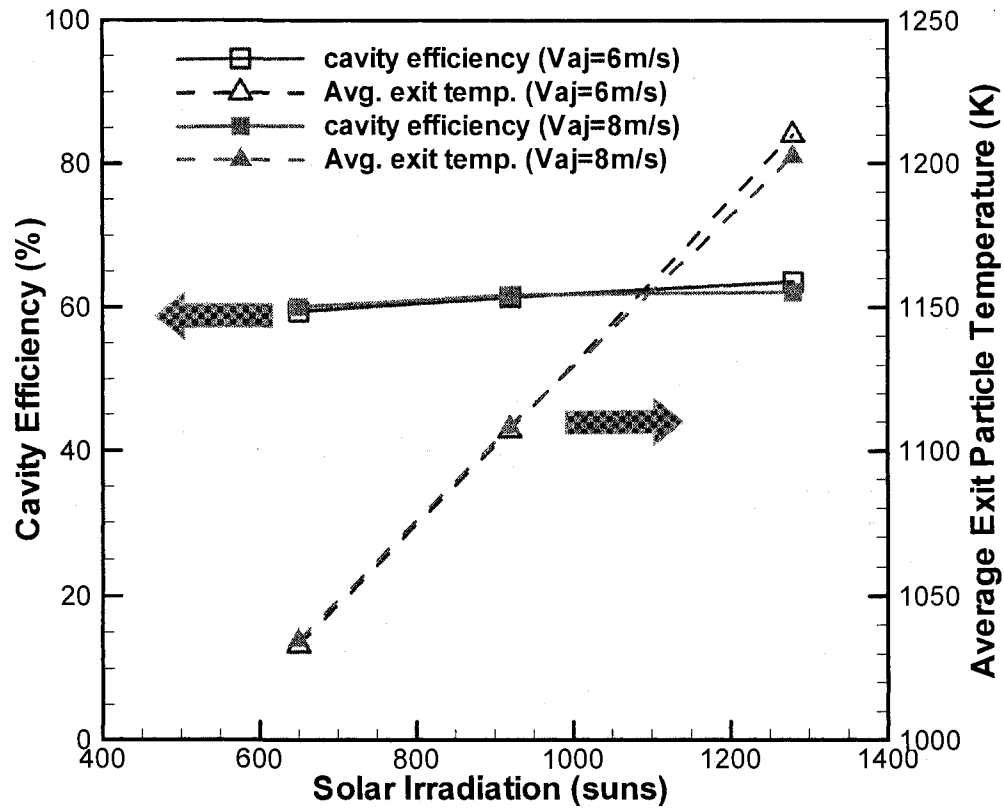


Figure 4. 25 Cavity efficiency and average exit particle temperature as a function of different solar irradiation values, downward air-jet temperature is 300 K, diameter of particle is 650 micron, and mass flow rate is 5 kg/s

CHAPTER 5

CONCLUSIONS AND RECOMMENDATION

5.1 Conclusions

This research presents the following results on the simulation of a SPSR with the influence of an air-jet. Using a CFD technique a parametric study of the aerodynamic behavior is investigated in this research. The simulation results are aimed at providing the useful information to lead the design of a high performance SPSR. This paper explains the following major problems:

- (1) Generate a three-dimensional numerical model for solid particle solar receiver.
- (2) Compare SPSR cavity efficiency and average exit particle temperature with and without an air-jet.
- (3) Identify the optimized operation conditions of the SPSR, including: air-jet velocity, air-jet temperature, particle size, particle mass flow rate, and solar flux value.

The numerical results obtained in this research provide a better idea for the design process and the experimental research. They also provide insight in to how to improve the design of the SPSR.

The computational fluid dynamics analysis of the SPSR without an air-jet and with different air-jet velocities is presented in this study. A two way coupling Euler-

Lagrange method was used to simulate the gas phase and solid particle flow inside the cavity. The solar ray tracing and discrete ordinate model evaluate the flow pattern, velocity, and efficiency inside the SPSR. The profiles for demonstrating the gas and particle aerodynamics and thermal behaviors are studied in detail. The parametric studies on the air-jet influence on SPSR provide better ideas on the method to increase the cavity efficiency, by modifying the design to optimize the SPSR performance.

The efficiency of the particle receiver and the particle exit temperature will increase by applying an air-jet design. The application of an air-jet can block the heat convection loss compared to the case without an air-jet, for the purpose of reducing the convection and radiation loss. A velocity of 8 m/s for the air-jet provides fairly good screening result, over the selected range of 0 m/s to 10 m/s. Increasing the particle mass flow rate leads to increased cavity efficiency, and decreased average exiting particle temperature. Through applying smaller particle size in the SPSR, a higher exiting particle temperature and efficiency is achievable. And particle with diameter of 70-80 micron is the optimized size that gives the best performance of SPSR. This particle size with a downward air-jet temperature of 300 K, air-jet velocity of 8 m/s, mass flow rate of 5 kg/s, and under the solar radiation of 920 suns, can bring the cavity efficiency of 85 % and average exit particle temperature of 1199 K, which proves this conceptual design of SPSR can achieve the minimum temperature requirement for the thermo-chemical reaction. On the other hand, using a heated air-jet to cover the aperture cannot help to improve cavity efficiency. This phenomenon was caused by the buoyancy force which acted on the pre-heated air-jet. Also the pre-heat air-jet injected from the bottom of the

cavity doesn't influence the performance of SPSR. Higher solar flux radiation will give a better performance on the heat absorption.

5.2 Future Work

For the future studies related to this research, a few improvements can be realized, and the simulation results can be more reasonable. The recommended improvements of SPSR for the future study are as follows:

- (1) Consider the wind influence combined with the performance of an air-jet.
- (2) The boundary condition on the cavity wall is more reasonable if one considers the conduction effect.
- (3) Heat inside the cavity can be recuperated.

REFERENCES

- [1] Stephane Abanades, P. Chsrvin, G. Flamant, and P. Neveu, 2006, "Screening of water-splitting thermochemical cycles potentially attractive for hydrogen production by concentrated solar energy," *Energy*, Vol.31, pp.2805-2822.
- [2] Thomas Rostrup-Nielsen, 2005, "Manufacture of hydrogen," *Catalysis Today*, Vol.106, pp.293-296.
- [3] Koroneos C, Dompros A, Roumbas G, Moussiopoulos N, 2004, "Life cycle assessment of hydrogen fuel production processes," *Int. J. Hydrogen Energy*, Vol. 29, pp.1443-1450.
- [4] Huang, C., T- Raissi, A, "Analysis of Sulfur-Iodine Thermochemical Cycle for Solar Hydrogen Production. Part I: Decomposition of Sulfuric Acid," *Solar Energy*, vol. 78(5), pp. 632-646, 2005.
- [5] Summers, W.A, Gorenssek, M.B. "Nuclear hydrogen production based on the hybrid sulfur thermochemical process," 2006, *Proceeding of the 2006 International Congress on Advances in Nuclear Power Plants*, Vol.2006, pp. 2254-2256.
- [6] Steinfield, A., "Solar hydrogen production via a two step water splitting cycle based on Zn/ZnO redox reaction," 2002, *Int.J.Hydrogen Energy*, Vol.27, pp.611-619.
- [7] J. Hraby, R. Steeper, G. Evans, C. Crowe. "An experimental and numerical study of flow and convective heat transfer in a freely falling curtain of particles," 1988, *Journal of Fluids Engineering*, Transaction of the ASME, Vol.110, pp. 172-181.

- [8] Gregory H. Evans, William G. Houf, "Numerical modeling of a solid particle solar central receiver," 1985, Sandia National Laboratories, Sandia report, SAND85-8249.
- [9] Robert T. Taussig, 1984, "Aerowindow for Center Solar Receivers," ASME, 84-WA/Sol-14, pp. 1-12.
- [10] O'Keefe D. Allen C, Besenbrush G, Brown L, Norman J, Sharp R, 1982, "Preliminary results from bench-scale testing of a sulfur-iodine thermochemical water-splitting cycle," Int. J. Hydrogen Energy, 7:381-92.
- [11] Ozturk IT, Hammache A, Bilgen E, 1995, "An improved process for H_2SO_4 decomposition step of the sulfur-iodine cycle," Energy Convers Manage, Vol. 36(1), pp 11-21.
- [12] Cunping Huang, Ali T-Raissi, 2005, "Analysis of sulfur-iodine thermochemical cycle for solar hydrogen production. Part I: decomposition of sulfuric acid," Solar Energy, Vol. 78, pp. 632-646.
- [13] N.P. Siegel, G.J. Kolb, 2007, "Solid particle receiver flow characterization studies," ES2007-36118, Energy Sustainability 2007.
- [14] Steinfeld, A., Imhof, A., and Mischler, D., 1992, "Experimental investigation of an atmospheric-open cyclone solar reactor for solid-gas thermochemical reactions," ASME Journal of Solar Energy Engineering, Vol.114, pp.171-174.
- [15] Steinfeld, A., Frei, A., Kuhn, P., and Wullemmin, D., 1995, "Solar thermal production of zinc and syngas via combined ZnO-reduction and CH_4 -reforming processes," International Journal of Hydrogen Energy, Vol.20, pp.793-804.

- [16] Haueter, P., Moeller, S., Palumbo, R., and Steinfeld A.,1999. "The production of zinc by thermal dissociation of zinc oxide solar chemical reactor design," *Solar Energy*, Vol.67, pp.161–167.
- [17] Hirsch, D., Steinfeld, A., 2004, "Radiative Transfer in a Solar Chemical Reactor for the Co-Production of Hydrogen and Carbon by Thermal Decomposition of Methane," *Chemical Engineering Science*, Vol. 59, pp 5771-5778.
- [18] A. Meier, J. Ganz, A, Steinfeld, 1996, "Modeling of a novel high-temperature solar chemical reactor," *Chemical Energy Science*, Vol.51, No.11, pp.3181-3186.
- [19] A. Meier, 1999, "A predictive CFD model for a falling particle receiver/reactor exposed to concentrated sunlight," *Chemical Engineering Science*, Vol. 54, pp. 2899-2905.
- [20] Hanna H. K., Jacob K., Rami B., Rudi B. 2007, "Heat transfer in a directly irradiated solar receiver/reactor for solid-gas reactions," *Solar Energy*, Vol.81, pp.1227-1239.
- [21] C. T. Crowe, M. P. Sharma, D. E. Stock, 1977, "The particle-source-in cell (PSI-CELL) model for gas-droplet flows," *Journal of Fluid Engineering*, June, pp. 325-332.
- [22] G. D. Raithby, E. H. Chui, 1990, "A finite-volume method for predicting a radiant heat transfer in enclosures with participating media," *Journal of Heat Transfer*, Vol. 112, pp.415-423.
- [23] H. K. Versteeg, W. Malalasekera, 1995, "An introduction to computational fluid dynamics," Pearson-Prentice Hall.
- [24] W. P. Jones, B. E. Launder, 1971, "The prediction of laminarization with a two-equation model of turbulence," *Int. J. Heat Mass Transfer*, Vol. 15, pp. 301-314.

- [25] J. A. C. Humphrey, W. M. To, 1986, "Numerical simulation of buoyant, turbulent flow-I. Free convection along a heated, vertical, flat plate," *Int. J. Heat Mass Transfer*, Vol.29, No. 4, pp. 573-592.
- [26] J. A. C. Humphrey, W. M. To, 1986, "Numerical simulation of buoyant, turbulent flow-II. Free and mixed convection in a heated cavity," *Int. J. Heat Mass Transfer*, Vol.29, No. 4, pp. 593-610.
- [27] N. Z. Ince, B. E. Launder, 1989, "On the computation of buoyancy-driven turbulent flows in rectangular enclosures," *Int. J. Heat and Fluid Flow*, Vol. 10, No. 2. pp. 110-117.
- [28] Tsah-Hsing S., William W. L., Aamir S., Zhigang Y, and Jiang Z., 1995, "A new $\kappa - \varepsilon$ eddy viscosity model for high Reynolds number turbulent flows," *Computers Fluids*, Vol. 24, No. 3, pp. 227-238.
- [29] G. H. Evans, W. G. Houf, "Numerical modeling of a solid particle solar central receiver," Sandia National Laboratories, Sandia report, SAND85-8249.
- [30] Huajun Chen, Yitung Chen, and Hsuan-Tsung Hsieh, "Computational Fluid Dynamics Modeling of Gas-Particle Flow Within a Solid-Particle Solar Receiver," *Journal of Solar Energy Engineering*, May 2007, Volume 129, Issue 2, pp. 160-170.
- [31] Abdelrahman, P., Fumeaux, P., and Suter, P., 1979, "Study of solid-gas suspension used for direct absorption of concentrated solar radiation," *Solar Energy*, Vol. 22, pp.45-48.
- [32] Hruby, J.M., "A technical feasibility study of a solid particle solar central receiver for high temperature applications," Sandia National Laboratories, Sandia report, SAND86-8211.

- [33] Hruby, J.M., and Burolla, V.P., 1984, "Solid particle receiver Experiments: Velocity Measurements," Sandia National Laboratories, SAND84-8238.
- [34] H. C. Van der Hulst, 1957, "Light Scattering by Small Particles," Wiley, New York.
- [35] Stahl, K.A., Griffin, J. W., Matson, B.S., Pettit, R. B., 1986, "Optical characterization of solid particle solar central receiver materials," Sandia National Laboratories, SAND 85-1215, 1986.
- [36] Patankar S.V., 1980, "Numerical heat transfer and fluid flow," Hemisphere, New York.
- [37] Fluent Inc., 2005, "Fluent users guide, version 6.3.26." Lebanon, USA.
- [38] Clift, R., Grace, J.R., and Weber, M.E., 1978, "Bubbles, drops and particles," London: Academic Press.
- [39] T. J. Barth and D. Jespersen, 1989, "The design and application of upwind schemes on unstructured meshes," Technical Report AIAA-89-0366, AIAA 27th Aerospace Sciences Meeting, Reno, Nevada.
- [40] T. Tan, Y. Chen, and Z. Chen, 2008, "Numerical Investigation of Influences of an Aerowindow on the Performance of Solid Particle Receivers," Solar 2008-0239, May 3-8, San Diego, CA, USA.
- [41] Z. Chen, Y. Chen, and T. Tan, 2008, "Numerical Analysis on the Performance of the Solid solar Particle Receiver with the Influence of Aerowindow," ASME Fluids Engineering Division Summer Conference, FEDSM 2008-55285, Aug 10-14, 2008, Jacksonville, Florida, USA.

VITA

Graduate College
University of Nevada, Las Vegas

Zhuoqi Chen

Local Address:

1600 E. University Ave, Apt 220
Las Vegas, NV 89119

Degree:

Bachelor of Engineering, Electrical Engineering, 2006
Hangzhou Dianzi University, China.

Selected publications:

- Zhuoqi Chen, Yitung Chen, and Taide Tan, "Numerical Analysis on the Performance of the Solid solar Particle Receiver with the Influence of Aerowindow," *ASME Fluids Engineering Division Summer Conference, FEDSM 2008-55285*, Aug 10-14, 2008, Jacksonville, Florida, USA.
- Taide Tan, Yitung Chen, and Zhuoqi Chen, "Wind Effect on the Performance of Solid Particle SOLAR Receivers: Part II-The Performance with an Aerowindow Protection," submitted to *solar energy*, June 2008, (under reviewing).
- Taide Tan, Yitung Chen, and Zhuoqi Chen, "Wind Effect on the Performance of Solid Particle SOLAR Receivers: Part I- The Models and the Performance without an Aerowindow Protection," submitted to *solar energy*, June 2008, (under reviewing).

Thesis Title:

Numerical Analysis of the Solid Particle Receiver with the Influence of an Air-jet

Thesis Examination Committee:

Chairperson, Dr. Yitung Chen, Ph.D.
Committee Member, Dr. Robert Boehm, Ph. D.
Committee Member, Dr. Daniel Cook, Ph. D.
Graduate College Representative, Dr. Jichun Li, Ph. D.